crystals

MDPI

Review

$(Li_{1-x}Fe_x)OHFeSe$ Superconductors: Crystal Growth, Structure, and Electromagnetic Properties

Guo-Yong Zhang [1], Mitch Ming-Chi Chou [1,2] and Cheng-Tian Lin [1,*]

[1] Max Planck Institute for Solid State Research, D-70569 Stuttgart, Germany; gyzhang2@gmail.com (G.-Y.Z.); mitch@faculty.nsysu.edu.tw (M.M.-C.C.)

[2] Department of Materials and Optoelectronic Science, National Sun Yat-Sen University, Kaohsiung 80424, Taiwan

* Correspondence: ct.lin@fkf.mpg.de; Tel.: +49-711-689-1458; Fax: +49-711-689-1093

Academic Editor: Haidong Zhou

Received: 28 March 2017; Accepted: 3 June 2017; Published: 6 June 2017

Abstract: This review focuses on the growth of high-quality $(Li_{1-x}Fe_x)OHFeSe$ single crystals by a hydrothermal method using floating-zone-grown $A_xFe_{2-y}Se_2$ (A = K, Rb, and Cs) as precursors. The structure, superconductivity, and magnetic behavior of the obtained crystals are highly influenced by the growth conditions, such as time, temperature, and composition. A phase diagram with temperature against the c-lattice constant is summarized including the antiferromagnetic spin density wave, superconducting, and paramagnetic phases.

Keywords: iron-based superconductor; $(Li_{1-x}Fe_x)OHFeSe$ single crystal; hydrothermal growth; optical floating-zone growth; self-flux growth; Bridgman growth; high-temperature superconductivity; spin density wave; phase diagram; anisotropy

1. Introduction

Iron-based superconductors (FeSCs) have attracted much attention because of their diverse structures, complex phases, and unconventional superconductivity [1–16]. FeSCs have the highest superconducting (SC) transition temperatures (T_c) after cuprate SCs, above the generally accepted McMillan limit of 39 K predicted by Bardeen–Cooper–Schrieffer (BCS) theory, opening up new opportunities for exploring novel high-T_c SCs [17].

The crystal structure of FeSCs characteristically consists of some kind of stacking layers which conduct the SC current [18]. In iron-arsenide and iron-selenide, compounds that have been most widely studied, the alternately stacked Fe_2X_2 (X = As and Se) layers are formed by edge-sharing disordered FeX_4 tetrahedra, which leads to them sharing many similar structures and properties [19]. Up to now, several types of iron-arsenide SCs have been discovered, including Fe_2As-type AFeAs (111-system, A is Li or Na) [20–22], $ThCr_2Si_2$-type $Ae Fe_2As_2$ (122-system, Ae is an alkaline or alkaline-earth metal element) [23,24], ZrCuSiAs-type ReFeAsO, Co doped AeFFeAs (1111-system, Re is a rare-earth element) [25–27], and the perovskite-based materials such as $(Sr_4M_2O_6)(Fe_2Pn_2)$ (42622-system; M = Sc, Ti, and V; Pn = P and As) [28,29], and $(Ca_3Al_2O_{5-y})(Fe_2Pn_2)$ (32522-system) [30]. At ambient pressure, T_c reaches as high as 55 K and 56 K in $SmO_{1-x}F_xFeAs$ and $Sr_{1-x}Sm_xFFeAs$, respectively [31,32]. Since their discovery, iron-selenide SCs have been found to provide a strong platform for the investigation of their high-T_c superconductivity, since they possess a simple structure, are nontoxic, and may be fabricated via numerous synthesis methods [2,18,33,34]. The simplest tetragonal β-$Fe_{1+\delta}Se$ (11-system) has $T_c \approx 8.5$ K at ambient pressure and is sensitive to chemical and physical pressure effects [35]. It was observed that T_c can be increased up to 15 K in the β-$Fe_{1+\delta}Se$ system by partially replacing Se with Te and up to 36.7 K under the application of a hydrostatic pressure of 8.9 GPa [36,37]. The positive pressure coefficient dT_c/dP reaches as high as 9.1 K/GPa for this system, although smaller than

$|-(60 \pm 3)|$ K/GPa for $Ca(Fe_{1-x}Co_x)_2As_2$ [38,39]. In contrast to the negatively charged FeAs layers in iron arsenide systems, the anti-PbO-type FeSe layers are charge neutral, and the excess Fe is important to the phase diagram and structural stability of the β-$Fe_{1+\delta}Se$ system [40]. The two adjacent FeSe layers are weakly coupled and are susceptible to intercalation, which can improve the superconductivity of the system by modulating the crystal lattice constants or even by changing the crystal structure [40,41]. A series of new SCs with T_c about 30 K have been fabricated by the intercalation of metal ions and small molecules, including $A_xFe_{2-y}Se_2$ [A = K, Rb, Cs, (Tl,K), and (Tl,Rb)] [42], $M_x(NH_3)_yFe_2Se_2$ (M: metal elements) [43,44], $Li_x(NH_2)_y(NH_3)_{1-y}Fe_2Se_2$ [45], and $Li_x(C_5H_5N)_yFe_{2-z}Se_2$ [46]. Besides the coexistence of superconductivity and ferromagnetism, a variety of phase separation phenomena have been observed in these SCs [18]. It was reported that two SC phases with T_c of 44 K and 30 K coexist in $K_{0.4}Fe_2Se_2(NH_3)_{0.5}$ [47]. In polycrystalline $Fe(Se_{1-x}Te_x)_{0.82}$ ($0.15 \leq x \leq 0.3$), there are also two different SC phases, arising from two tetragonal structures with the same space group but different lattice parameters [48]. In the $A_xFe_{2-y}Se_2$ system, intrinsic phase separation in coexisting crystallographic phases is a common feature [18]. The majority phase $A_{0.8}Fe_{1.6}Se_2$ (the so-called '245' phase) is antiferromagnetic (AFM) with large magnetic moments of 3.31 μ_B per Fe and a Néel transition temperature (T_N) up to 560 K. It shows an insulating/semiconducting behavior accompanied by Fe-vacancy orders with a $\sqrt{5} \times \sqrt{5}$ superstructure. Embedded in the 245 phase is the minority metallic-SC phase which is Fe vacancy free with the formula $A_{1-x}Fe_2Se_2$ ($0 \leq x \leq 0.7$) [49]. Direct observation shows that the phase separation in a $K_xFe_{2-y}Se_2$ single crystal at temperatures below 520 K is characterized by the coexistence of the majority tetragonal magnetic phase, minority orthorhombic metallic phase, and an interfacial tetragonal phase which appears below ~300 K [50]. However, the coexistence of these complex microstructures makes it difficult to grow bulk SC $A_xFe_2Se_2$ single crystals and hinders the determination of their intrinsic electrical and magnetic properties [51].

Recently, $(Li_{0.8}Fe_{0.2})$OHFeSe (11111-system) polycrystalline SCs with T_c ~ 40 K were synthesized using a hydrothermal method [52]. This new FeSe-derived SC material has an alternate stacking of anti-PbO-type FeSe layers and $(Li_{0.8}Fe_{0.2})$OH layers, with a weak interlayer hydrogen bonding interaction. Compared with β-$Fe_{1+\delta}Se$, the $FeSe_4$ tetrahedron in the *ab* plane in $(Li_{0.8}Fe_{0.2})$OHFeSe is highly compressed, which is believed to play a key role in enhancing superconductivity. In contrast, the ideal $FeAs_4$ tetrahedron is favorable for superconductivity in FeAs-based SCs. In $(Li_{0.8}Fe_{0.2})$OHFeSe, the electron-type carriers dominate the conduction, and a canted AFM order occurs at ~8.5 K, coexisting with superconductivity at ~40 K. Moreover, $(Li_{0.8}Fe_{0.2})$OHFeSe is stable in air, unlike other FeSe SCs intercalated with alkali metal ions, NH_3 molecules, or organic molecules, which are extremely air sensitive. Soon after the synthesis of polycrystalline $(Li_{1-x}Fe_x)$OHFeSe via a hydrothermal method, $(Li_{1-x}Fe_x)$OHFeSe single crystals with T_c above 44 K were successfully synthesized via a hydrothermal ion-exchange process using $A_xFe_{2-y}Se_2$ (A = K, Rb, and Cs) as precursors, in which the 245 phase is absent [53]. They have a narrow SC transition and 100% shield volume fractions, indicating their excellent bulk superconductivity; in contrast, the shield fractions of $A_xFe_{2-y}Se_2$ are only 10–20% [47]. These advantages make the $(Li_{1-x}Fe_x)$OHFeSe crystal an ideal system for investigating the intrinsic mechanism behind its superconductivity and the effect of anisotropy in its crystal structure on its superconducting properties. In this article, we review the growth technology, structure, and physical properties of $(Li_{1-x}Fe_x)$OHFeSe single crystals.

2. Crystal Growth

2.1. $A_xFe_{2-y}Se_2$ (A = K, Rb, and Cs) Precursor

$A_xFe_{2-y}Se_2$ (A = K, Rb, and Cs) single crystals used as precursors can be obtained using self-flux, Bridgman, and optical floating-zone (OFZ) crystal growth methods [54–63]. Figure 1a,b show the schematic illustrations of the self-flux and Bridgman growth methods, respectively. A typical procedure for the self-flux growth method is as follows [56,63]. First, the FeSe precursor was prepared by reacting Fe and Se powders at 700 °C for 4 h in an evacuated quartz tube. Then, the obtained FeSe precursor

was ground into powder and mixed with A (A = K, Rb, and Cs) pieces at a ratio of A:FeSe = 0.8:2. The mixtures were put into a double-sealed quartz ampule which would protect the raw materials from exposure to air, in case the inner tube broke during growth. The samples were heated to 1030 °C in 4 h and kept at this temperature for 2 h. Before the furnace was shut down at 750 °C, either a cooling rate of 6 °C/h or a quenching method was applied. The actual compositions of $K_xFe_2Se_2$ and $Cs_xFe_2Se_2$ were determined to be K:Fe:Se = 0.75:1.66:2 and Cs:Fe:Se = 0.81:1.61:2, respectively [56]. In addition, it was reported that using a Bridgman method, $A_xFe_{2-y}Se_2$ single crystals were grown when the melt was soaked at 1070 °C for 5 h and a slow traveling speed of 3 mm/h was applied [62]. Using the starting mixture Rb:FeSe = 1:2.5, the actual compositions of the obtained crystal were determined to be Rb:Fe:Se = 0.740(36):1.600(6):2.000(25) [62].

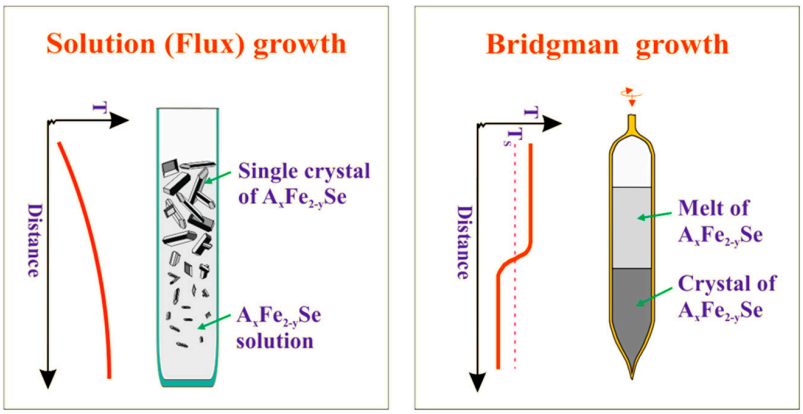

Figure 1. Schematic illustrations of the (**a**) self-flux; and (**b**) Bridgman growth methods.

The OFZ crystal growth method is unique in growing both congruent and incongruent melt compounds without contamination of crucible materials. This also allows the production of large crystals that cannot be obtained using solution methods. The relatively high thermal gradient at the crystallization front can be used to control the extent of the constitutional supercooling and has the advantage of a rapid growth of crystals from an incongruent melt. The OFZ method has been successfully used to grow large and high-quality single crystals of high-T_c superconductors, including FeSCs such as $A_xFe_{2-y}Se_2$ (A = K, Rb, and Cs) [2,63–77]. Figure 2 shows a schematic illustration of the OFZ growth setup and snapshot of the real growth process. The feed rod was prepared via a one-step conventional solid-state reaction as reported in Ref. [63]. Elemental A, Fe, and Se were mixed with the nominal molar ratio of A:Fe:Se = 0.8:2:2 and sintered at 850 °C for 10 h. After sintering, the $A_{0.8}Fe_2Se_2$ mixture was uniformly ground into powder, which was pressed into a feed rod of ~70–80 mm in length and ~6–7 mm in diameter using a hydraulic press under an isostatic pressure of 600 bar. The feed rod was used to grow the crystal directly, without the conventional sintering or pre-melting process. A seed rod of 2 cm in length was obtained by cutting the feed rod. The $A_xFe_{2-y}Se_2$ single crystals were grown in a four-mirror OFZ furnace (FZ–T–10000–H–III–VPR, Crystal System Inc., Salem, MA, USA) having four 300 W halogen lamps as the heating source. Rotation rates of 20 rpm were employed for both the feed and seed shafts in opposite directions. Growths were carried out at a travelling velocity rate of 0.8 mm/h under an 8 bar argon atmosphere. The obtained crystals were large and homogeneous with a mass of up to 1.8 g. Figure 3a shows a schematic illustration of the OFZ growth process for the $A_xFe_{2-y}Se_2$ single crystals. It was found that as the molten zone was slowly moved up along the length of the rotating feed rod, the grown crystal continuously passed through a special temperature zone, T_d, where it began to decompose. Therefore, to protect the grown crystal, the four halogen lamps were turned off towards the end of the crystal growth, resulting in un-destroyed crystal phase at the upper portion of the grown ingot. Figure 3b–d shows the typical as-grown single-crystal ingots of

$K_{0.80}Fe_{1.81}Se_2$, $Rb_{0.80}Fe_{1.81}Se_2$, and $Cs_{0.80}Fe_{1.81}Se_2$, respectively. It can be seen in the inset of Figure 3b that the cleaved ingot displays a large crystal grain with a flat shiny surface. It is interesting to find that although the A ions are different, the iron content in all the $A_xFe_{2-y}Se_2$ crystals is approximately 1.81, which is higher than for the ones grown by the self-flux and Bridgman methods. In addition, it was observed that the Fe content in the crystals can be adjusted by changing the growth atmospheres.

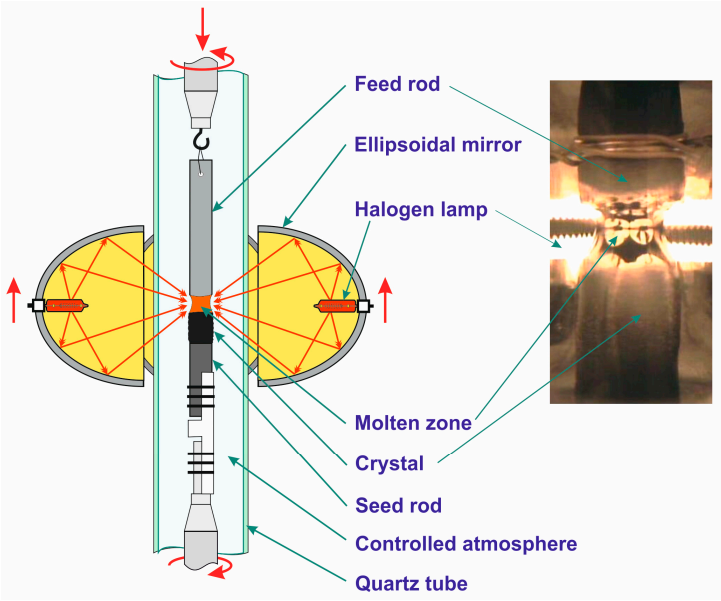

Figure 2. Optical floating-zone (OFZ) growth setup (**left**); and snapshot (**right**) of the real iron-based superconductor growth process.

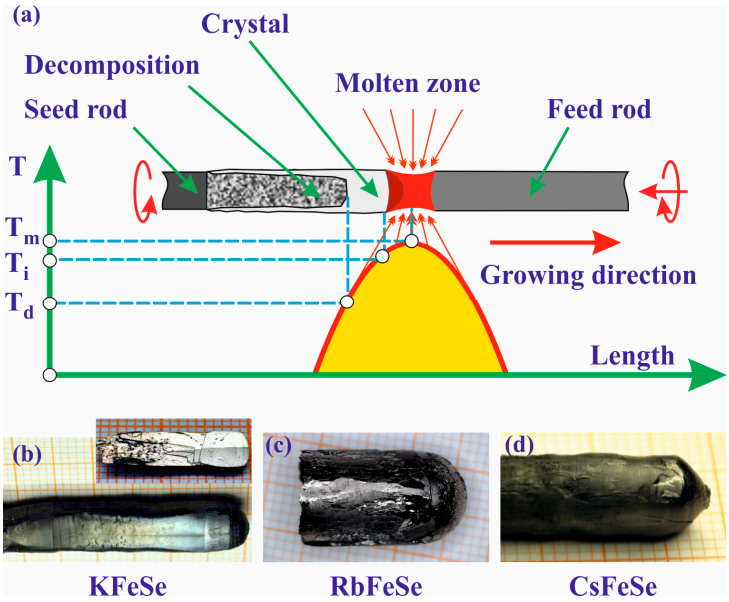

Figure 3. (**a**) Schematic drawing illustrates the OFZ growth process of the $A_xFe_{2-y}Se_2$ single crystals, which form between the solid–liquid interface temperature (T_i) and the decomposition temperature (T_d), below which the crystals undergo a continuous decomposition during the molten zone traveling; (**b**) a typical as-grown $K_{0.80}Fe_{1.81}Se_2$ single-crystal ingot. Inset shows a crystal cleaved along the growing direction; (**c**,**d**) single crystals cut off from ingots of $Rb_{0.80}Fe_{1.81}Se_2$ and $Cs_{0.80}Fe_{1.81}Se_2$, respectively.

2.2. Hydrothermal Growth

The hydrothermal method is an important method of crystal growth that is complementary to the classical melt-based or vapor transport methods, being widely used to synthesize new materials, new structures, and new phases for various applications [78]. This method is available for preparing novel SCs, such as $Ba_{1-x}K_xBiO_3$ [79], $Ba_{1-x}K_xBi_{1-y}Na_yO_3$ [79], $BaPd_{1-x}Bi_xO_3$ [80], and La_2CuO_{4+y} [81]. Recently, the hydrothermal growth of $(Li_{1-x}Fe_x)$OHFeSe single crystals has been reported [53]. The crystal precursors were prepared by cleaving the OFZ-grown single crystals of $A_xFe_{2-y}Se_2$ (A = K, Rb, and Cs) [63]. $C(NH_2)_2Se$ (99.95%), Fe powder (99.995%), LiOH (99.95%), and 9 mL H_2O with a mol ratio of Se:Fe:Li = 1:4.38:51.47–154.41 were used for preparing the mixtures. Both the crystal precursors and the mixtures were tightly sealed in a Teflon-lined steel autoclave (30 mL) prior to being heated in a box furnace from room temperature to 120–180 °C at a rate of 60 °C/h. The crystal precursors and mixtures were held at the temperature for up to 4 d, before cooling down naturally to room temperature. The large as-grown $(Li_{1-x}Fe_x)$OHFeSe single crystals were separated and washed several times with methanol solution to obtain clean surfaces. Figure 4a,b show the Teflon-lined hydrothermal synthesis autoclave reactor and the growth procedure, respectively. Similar hydrothermal growth methods have been used to prepare $(Li_{1-x}Fe_x)$OHFeSe materials, but, the precursor chosen has significant effects on the final products. Using tetragonal FeSe as the precursor, small (~10 × 10 × 1 μm) crystals were grown [82]. Without using any precursor, polycrystalline samples were obtained [52].

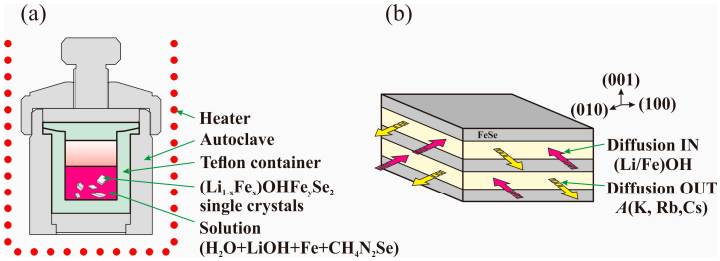

Figure 4. Growth of $(Li_{1-x}Fe_x)$OHFeSe single crystals via hydrothermal ion exchange. (**a**) Schematic apparatus of the autoclave used for the crystal growth; (**b**) illustration of the Li/Fe–O–H ions diffusing in between the FeSe layers and the A ions diffusing out from the $A_xFe_{2-y}Se_2$ (A = K, Rb, and Cs) precursors during the hydrothermal growth process [53]. Reprinted with permission from IOP. All rights reserved.

2.3. Crystal Characterization Techniques

The $(Li_{1-x}Fe_x)$OHFeSe and $A_xFe_{2-y}Se_2$ (A = K, Rb, and Cs) single crystals have been characterized by different kinds of techniques [2,52,53,63]. The actual composition of the crystals is determined by energy-dispersive X-ray (EDX) spectroscopy or more precise inductively coupled plasma atomic-emission spectroscopy (ICP-AES) analysis. The crystal structures are characterized by X-ray diffraction (XRD) and neutron powder diffraction (NPD). Electrical resistivity is measured by a standard four-probe technique to exclude the resistance of the leads using a physical properties measuring system (PPMS, Quantum Design). The contact resistance is smaller than 100 μΩ. Measurements of the magnetic susceptibility are investigated by a superconducting quantum interface device (SQUID) magnetometer (Quantum Design MPMS).

3. Crystal Structure

The final shape and size of the obtained $(Li_{1-x}Fe_x)$OHFeSe single crystals depends on the precursor crystals used. Thus, the large OFZ-grown $A_xFe_{2-y}Se_2$ (A = K, Rb, and Cs) crystal precursors used in the hydrothermal growth allows the preparation of large, high-quality $(Li_{1-x}Fe_x)$OHFeSe single crystals ~1 cm in diameter, as shown in Figure 5a. Due to the hydrothermal reaction, a thin layer

made from $[(Li_{1-x}Fe_x)OH](Fe_{1-y}Li_y)Se$ is usually deposited on the surface of the as-grown crystals, which shows T_c ~ 30–40 K with a broad transition [83], as shown in Figure 5b. When the deposited materials are carefully removed with Q-cotton in methanol, the black and plate-like crystal surface appears, as shown in Figure 5a. The as-grown crystals can be easily cleaved along the (001) direction, as shown in Figure 5c. This because that the *c*-axis is increased by 31%, since the adjacent edge-sharing $FeSe_4$ tetrahedra are linked to the intercalated $(Li_{1-x}Fe_x)OH$ layer via a much weaker hydrogen bonding interaction [52,53,65], however, the (001) plane, i.e., the surface of the crystal, is robust during the hydrothermal growth, as shown in Figure 5d. The as-grown crystals of $(Li_{1-x}Fe_x)OHFeSe$ are easily decomposed at room temperature, however, they are stable and can be stored in low-temperature environments like $[(Li_{1-x}Fe_x)OH](Fe_{1-y}Li_y)Se$ [83].

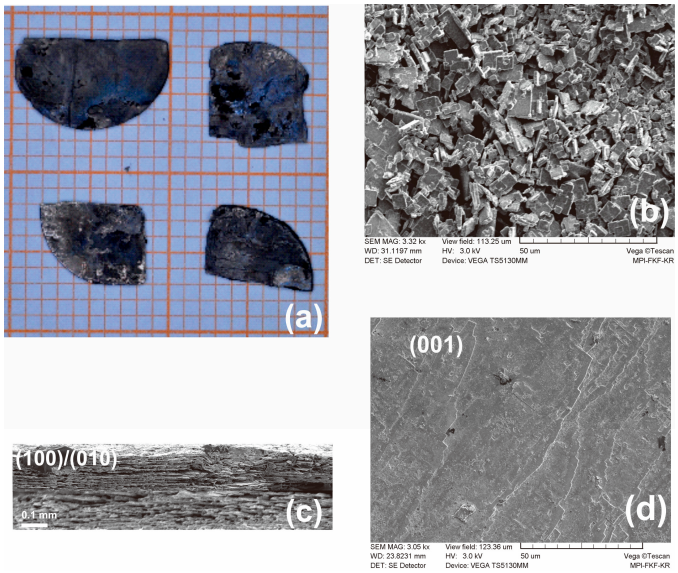

Figure 5. (**a**) As-grown ion-exchanged $(Li_{1-x}Fe_x)OHFeSe$ single crystals; (**b**) $[(Li_{1-x}Fe_x)OH](Fe_{1-y}Li_y)]Se$ by-products; (**c**) the (100)/(010) plane showing cracked layers along the (001) after ion exchange process; (**d**) the as-cleaned (001) surface after ion exchange process [53]. Reprinted with permission from IOP. All rights reserved.

Figure 6 shows the layered structure of the $(Li_{1-x}Fe_x)OHFeSe$ crystal. During the hydrothermal growth, intercalated $(Li_{1-x}Fe_x)OH$ layers are formed due to the ion exchange of *A* (K, Rb, and Cs). Along the *c*-axis anti-PbO type layers of $(Li_{1-x}Fe_x)OH$ alternate with anti-PbO type FeSe layers. In the hydroxide crystal, positively polarized hydrogen atoms of the $(Li_{1-x}Fe_x)OH$ layer point towards the negatively polarized selenium of the FeSe layer. The $(Li_{1-x}Fe_x)OH$ layer has a similar structure to LiOH itself, which likewise crystallizes in the anti-PbO-type [52,83].

The hydrothermal growth process induces a complete structural change. The obtained $(Li_{1-x}Fe_x)OHFeSe$ single crystals show an intergrowth of the ion-exchanged $(Li_{1-x}Fe_x)OH$ layers and the FeSe layers along the *c*-axis, which is greatly different from the structure of the $A_xFe_{2-y}Se_2$ (*A* = K, Rb, and Cs) crystals, representing an intergrowth of the iron-vacancy-ordered and -disordered states along the *c*-axis. Figure 7a–c show the XRD patterns of the $A_{0.80}Fe_{1.81}Se_2$ (*A* = K, Rb, and Cs) crystal precursors. In the three figures, the (00*l*) reflections demonstrating a tetragonal structure with space group $I4/m$ are related to the 245 insulating phase. The ordered and disordered iron vacancies along the *c*-axis in the $A_xFe_{2-y}Se_2$ crystals are characterized by slightly different lattice constants. It can be seen that there are three weak shoulders beside the (008), (00$\underline{10}$), and (00$\underline{12}$) reflections, as marked with the asterisks. The second set of the (00*l*) reflections with lower intensity is attributed to phase separation in the crystals [60]. The stronger reflections come from the superstructure, indicating that they are related to the iron vacancy-ordered insulating phase. Thus, the second phase marked with

asterisks must come from the minor metallic phase which is free of iron vacancy ordering, indicating that the crystal precursor only has a small volume (10%) of the SC phase [84]. However, only one set of the 00l (l = 2n) peaks is measured in ($Li_{1-x}Fe_x$)OHFeSe single crystals, indicating all of them are in a pure phase, as shown in Figure 7a–c.

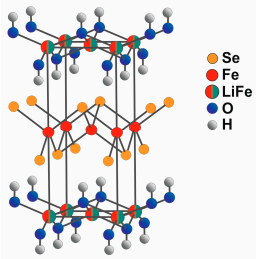

Figure 6. Crystal structure of ($Li_{1-x}Fe_x$)OHFeSe [53]. Reprinted with permission from IOP. All rights reserved.

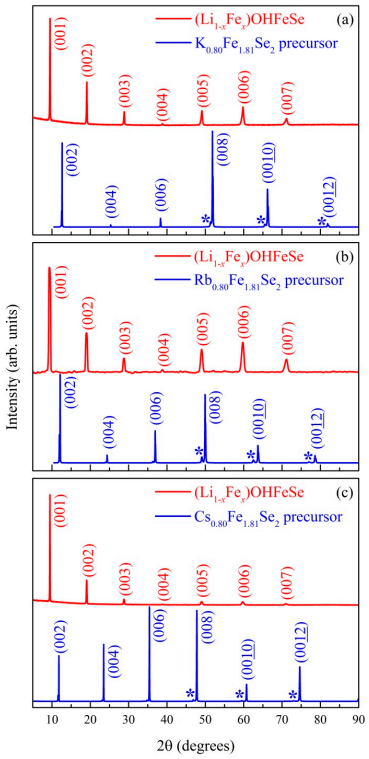

Figure 7. (**a**–**c**) The X-ray diffraction (XRD) patterns of the cleaved parent $A_{0.80}Fe_{1.81}Se_2$ (A = K, Rb, and Cs) and the ion-exchanged ($Li_{1-x}Fe_x$)OHFeSe crystals, respectively [53]. Reprinted with permission from IOP. All rights reserved.

Due to the hydrothermal ion exchange, it can be seen that all reflections related to the 245 insulating phase are absent, indicating that all $A_{0.80}Fe_{1.81}Se_2$ (A = K, Rb, and Cs) single crystals have been changed into ($Li_{1-x}Fe_x$)OHFeSe with its $P4/nmm$ space group, regardless of kind of A ion. The lattice parameters of the ($Li_{1-x}Fe_x$)OHFeSe produced using the $A_{0.80}Fe_{1.81}Se_2$ precursors are $a = b$ = 3.7862(7) Å, 3.779(1) Å, and 3.7693(0) Å, and c = 9.255(1) Å, 9.268(1) Å, and 9.281(7) Å, for A = K, Rb, and Cs, respectively. The c-axis lattice parameter increases with K, Rb, and Cs, which indicates that the larger ionic radius (R) provides more space, since R_K + (1.51 Å) < R_{Rb} + (1.61 Å) < R_{Cs} + (1.74 Å). It is reported that the lattice parameters from the NPD refinement of polycrystalline ($Li_{0.8}Fe_{0.2}$)OHFeSe at 2.5 K are $a = b$ = 3.77871(4) Å and c = 9.1604(1) Å [52]. For polycrystalline ($Li_{1-x}Fe_x$)ODFeSe with

x = 0.183(6), the Rietveld refinement of the neutron diffraction pattern collected at 4 K gave a = 3.7827(1) Å and c = 9.1277(3) Å [85]. The XRD measurement carried out at 298 K shows that a = 3.7865(2) Å and c = 9.2802(6) Å for polycrystalline $(Li_{0.8}Fe_{0.2})$OHFeSe [86]. These results show the lattice parameters are small at low temperatures.

Hydrothermal growth parameters greatly influence the structure and properties of the $(Li_{1-x}Fe_x)$OHFeSe single crystals. In order to find the optimum synthesis conditions, it is necessary to study the effects of the important growth parameters such as growth time (t), growth temperature (T_g), and the molar ratio of lithium ions (c_m) on c. Figure 8a–c show t, T_g, and c_m dependent XRD patterns, respectively [53]. The insets of the figures show the parameter dependence of c. In the experiments t, T_g, and c_m vary in the ranges 20–120 h, 120–200 °C, and 51.47–154.41 respectively, and c has the maximum value (c_{max}) as each parameter varies. For t and T_g, c_{max} is obtained in the medium parameter ranges, and c_{max} = 9.278(3) Å and 9.282(0) Å for t = 72 h and T_g = 160°C, respectively. For c_m, however, the c_{max} = 9.278(8) Å is obtained at the lowest c_m = 51.47. The maximum c_{max} = 9.282(0) Å is obtained as T_g = 160 °C. It is noted that as T_g, t, and c_m are adjusted the c values vary in the ranges 9.246(3)–9.282(0) Å, 9.255(1)–9.278(3) Å, and 9.262(3)–9.278(8) Å respectively, such that the range of variation in c due to changes in T_g spans the ranges of variation in c due to changes in t and c_m. Therefore, compared with t and c_m, T_g is more preferable for investigating the structural changes of the crystals, because by varying T_g both the highest values and the broadest distribution of c can be achieved at the same time. In addition, it is reported that reductive lithiation of the hydrothermally synthesized samples using lithium/ammonia solution can increase the c lattice parameter to obtain the SC phase [82].

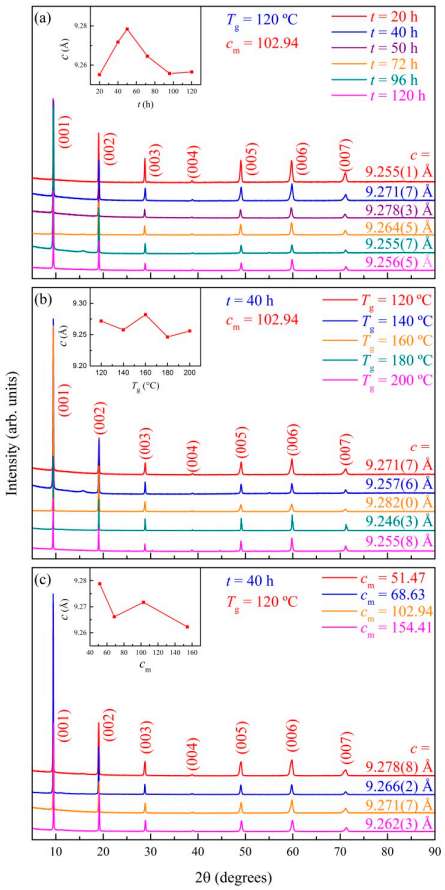

Figure 8. Dependence of the XRD patterns of the obtained $(Li_{1-x}Fe_x)$OHFeSe single crystals using the $K_{0.80}Fe_{1.81}Se_2$ precursors on (**a**) t, (**b**) T_g, (**c**) c_m. The insets show the effects of these three parameters on c, respectively [53]. Reprinted with permission from IOP. All rights reserved.

4. Superconductivity, Spin Density Wave, Antiferromagnetism and Ferromagnetism

Surprisingly, although the $A_{0.80}Fe_{1.81}Se_2$ (A = K, Rb, and Cs) precursors have very different properties, all the synthesized $(Li_{1-x}Fe_x)$OHFeSe crystals show enhanced SC properties, indicating that the intercalating layers play important roles in the high-T_c superconductivity mechanism [53].

Figure 9a–f show the electrical and magnetic properties of the $A_{0.80}Fe_{1.81}Se_2$ (A = K, Rb, and Cs) precursors and the $(Li_{1-x}Fe_x)$OHFeSe crystals. It can be clearly seen that the properties of the $A_{0.80}Fe_{1.81}Se_2$ (A = K, Rb, and Cs) precursors are different despite their similar structures.

The $K_{0.80}Fe_{1.81}Se_2$ precursor is a good superconductor, with a T_c of 31.76 (29.31) K derived from magnetic (electrical) measurements. After the hydrothermal ion-exchange process, its T_c is increased by 6.08 (13.38) K. Its zero field cooled (ZFC) susceptibility is nearly temperature independent before the onset of superconductivity, indicating that the normal state is Pauli paramagnetic, which can be found in the SC samples of $(Li_{1-x}Fe_x)$OHFeSe, $A_xFe_{2-y}Se_2$ (A = K, Rb, and Cs), and FeSe [3,7,56,62,87,88]. The hump peak of the normalized resistance versus temperature (R_{ab}/R_p–T) curve shifts from 220.79 K to 266.06 K and the resistivity of the hump peak is decreased from 560 mΩcm to 0.13 mΩcm due to the hydrothermal reaction. The peak-shift effect indicates that the SC/metallic property is improved. The SC transition width is defined as $\Delta T = T_c(\text{onset}) - T_c(0)$, where T_c(onset) is the temperature where the resistivity starts to deviate from the normal-state resistivity, and $T_c(0)$ is the temperature where zero resistivity state is achieved. For the $K_{0.80}Fe_{1.81}Se_2$ crystal precursor ΔT is 4.19 K, which is smaller than those for all the $(Li_{1-x}Fe_x)$OHFeSe crystals, indicating that some inhomogeneous structures resulting from the intercalating layers broaden the transition width.

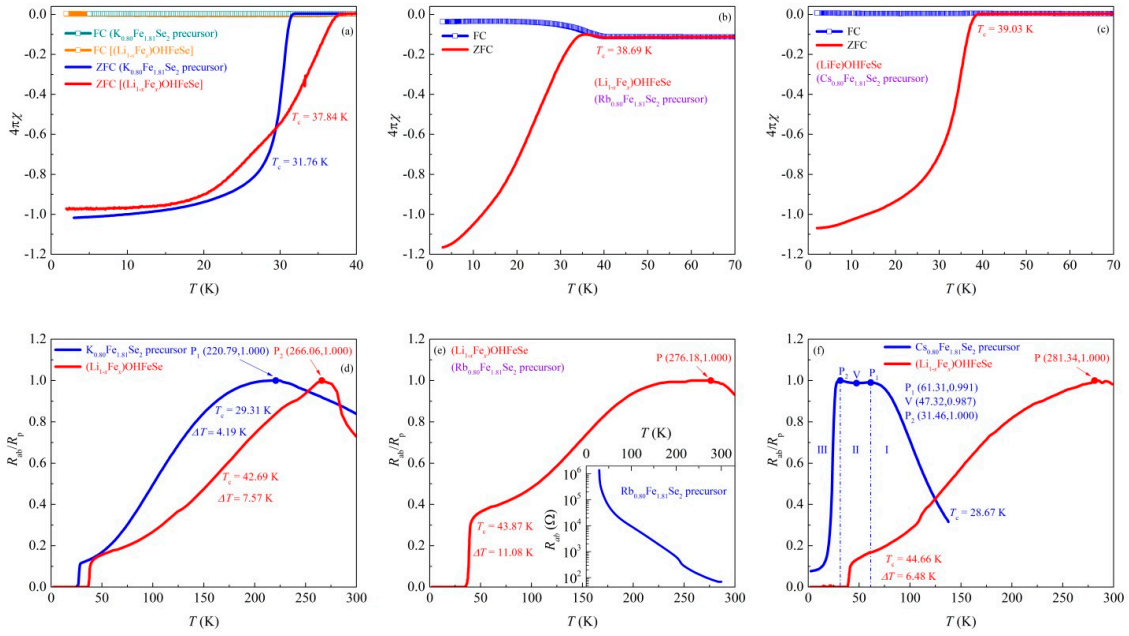

Figure 9. $4\pi\chi$–T curves for the (**a**) $K_{0.80}Fe_{1.81}Se_2$ precursor and $(Li_{1-x}Fe_x)$OHFeSe single crystal; (**b**) $(Li_{1-x}Fe_x)$OHFeSe single crystal using the $Rb_{0.80}Fe_{1.81}Se_2$ precursor; (**c**) $(Li_{1-x}Fe_x)$OHFeSe single crystal using the $Cs_{0.80}Fe_{1.81}Se_2$ precursor; R_{ab}/R_p–T curves for the (**d**) $K_{0.80}Fe_{1.81}Se_2$ precursor and $(Li_{1-x}Fe_x)$OHFeSe single crystal; the (**e**) $Rb_{0.80}Fe_{1.81}Se_2$ precursor and $(Li_{1-x}Fe_x)$OHFeSe single crystal; the (**f**) $Cs_{0.80}Fe_{1.81}Se_2$ precursor and $(Li_{1-x}Fe_x)$OHFeSe single crystal. R_{ab} is the the *ab*-plane resistance, and R_p is the maximum value of R_{ab} [53]. Reprinted with permission from IOP. All rights reserved.

The $Rb_{0.80}Fe_{1.81}Se_2$ precursor is non-conductive. As the temperature increases its resistance decreases monotonically and sharply, indicating that it acts as an electrical insulator.

The $Cs_{0.80}Fe_{1.81}Se_2$ precursor (T_c = 28.67 K) exhibits poor superconducting properties. Its resistance does not reach zero even at T = 2.53 K, but its R_{ab}/R_p is as high as 7.80%. Its electrical

transport properties are complex. It can be seen that its R_{ab}/R_p–T curve shows two hump peaks, P_1(61.31 K, 0.991) and P_2(31.46 K, 1.000), dividing the curve into three regions: high-, medium-, and low-temperature regions, which are denoted as 'I', 'II', and 'III', respectively. In region 'I', it shows semiconducting behavior. Additionally, the first peak P_1 is reached at T = 61.31 K, which is much smaller than those for the $K_{0.80}Fe_{1.81}Se_2$ crystal precursor and all the $(Li_{1-x}Fe_x)$OHFeSe crystals, indicating that an insulating/semiconducting phase is dominant in the high-temperature region. In region 'II', R_{ab}/R_p decreases with temperature because the metallic phase starts to play a role, and at the valley point 'V' (T = 47.32 K) the balance between the competitive conductive and non-conductive phases happens. After the 'V' point an unbalance occurs and thus the resistance increases again before the second hump peak 'P_2' is reached, where the SC state arises. In region 'III', the SC phase plays a leading role, and a sharp drop in resistance occurs after 'P_2' under the co-effects of the SC and metallic phases.

Despite the significant variation in the properties of the $A_{0.80}Fe_{1.81}Se_2$ (A = K, Rb, and Cs) precursors, high-quality $(Li_{1-x}Fe_x)$OHFeSe crystals with high T_c were obtained from all of them. The susceptibility measurements show that all the $(Li_{1-x}Fe_x)$OHFeSe crystals have high-temperature SC transitions, with T_c = 37.84 K, 38.69 K, and 39.03 K measured from samples produced from the $A_{0.80}Fe_{1.81}Se_2$ (A = K, Rb, and Cs) precursors, respectively. The superconductive shielding fraction estimated from the zero-field-cooling magnetization at T = 3 K is 97%, 100%, and 100% respectively, indicating the bulk superconductivity nature and high quality of the crystals. The electrical measurements show onset T_c = 42.69 K, 43.87 K, and 44.66 K respectively, confirming the SC transitions. Zero resistance of the $(Li_{1-x}Fe_x)$OHFeSe crystals grown using the $A_{0.80}Fe_{1.81}Se_2$ (A = K, Rb, and Cs) precursors is measured below 35.12, 32.79, and 38.18 K respectively, giving associated transition widths ΔT of 7.57 K, 11.08 K, and 6.48 K. In addition, it is found that the ionic radius of A^+ (R_A+) influences greatly the structures and properties of the $(Li_{1-x}Fe_x)$OHFeSe crystals. Both T_c and c increase with R_A+, suggesting that T_c depends on c. Among the $(Li_{1-x}Fe_x)$OHFeSe crystals, the crystal using the $Cs_{0.80}Fe_{1.81}Se_2$ precursor shows the best superconductivity: the highest T_c, the highest $T_c(0)$, and the narrowest ΔT. In addition, the R_{ab}/R_p–T curves of all the obtained crystals show a hump peak near room temperature, which is attributed to the doping effect of the $(Li_{1-x}Fe_x)$OH layers [82]. For the crystals made from the $A_{0.80}Fe_{1.81}Se_2$ (A = K, Rb, and Cs) precursors, the hump temperature T_h = 266.06, 276.18, and 281.34 K respectively. It shows that as R_A+ (or c) increases, T_h shifts toward high temperatures, indicating that the SC/metallic property is enhanced obviously in the crystals with the largest c-axis length, but the non-conductive property is weakened. Therefore, T_c increases due to the enhanced doping.

The $(Li_{1-x}Fe_x)$OHFeSe and the $A_xFe_{2-y}Se_2$ (A = K, Rb and Cs) crystals demonstrate complex electrical transport properties, which could be attributed to the doping effects of the $(Li_{1-x}Fe_x)$OH layer or A ions or the vacant sites in the FeSe layer [60,82,89]. However, using the same hydrothermal synthesis route, all $(Li_{1-x}Fe_x)$OHFeSe crystals have been synthesized with high superconductive shielding fraction and high T_c, despite the $A_{0.80}Fe_{1.81}Se_2$ (A = K, Rb, and Cs) precursors having significantly different properties that vary from being a good superconductor, to an insulator, and finally to a poor superconductor.

It is interesting to point out that SC and non-SC $(Li_{1-x}Fe_x)$OHFeSe single crystals can be selectively grown by controlling the growing parameters. SC crystals with large c-axis length can be prepared by a low-temperature hydrothermal reaction (e.g., 120 °C) or a high-temperature hydrothermal reaction for a short time (e.g., 160 °C for 40 h). In contrast, non-SC crystals with small c-axis length can be grown at high hydrothermal reaction temperatures for a long time (e.g., 180 °C and 72 h). Non-SC single crystals exhibit AFM spin density wave (SDW) transitions. Figure 10 shows the XRD patterns for a non-SC crystal prepared using a $Cs_{0.80}Fe_{1.81}Se_2$ crystal precursor. The inset shows that the AFM SDW transition temperature T_s = 125.41 K [53]. For polycrystalline $(Li_{1-x}Fe_x)$OHFeSe, the SC sample with T_c = 40 K was grown at 120 °C for 96 h, while the non-SC sample with T_s = 125 (127) K was grown at 160 (180) °C for 72 h [90].

In addition, the $(Li_{1-x}Fe_x)$OHFeSe provides a new platform to study the interplay between superconductivity and magnetism. It was reported that in polycrystalline $(Li_{0.8}Fe_{0.2})$OHFeSe superconductivity coexists with a field-induced ferromagnetism under external magnetic field and antiferromagnetism at zero field [52,91]. In $[(Li_{1-x}Fe_x)OH](Fe_{1-y}Li_y)Se$, superconductivity below T_c = 43 K coexists with ferromagnetism below 10 K [83]. The study of SC and non-SC $(Li_{1-x}Fe_x)OHFe_{1-y}Se$ suggests a glassy magnetic state, probably comprising clusters of iron ions of varying cluster sizes distributed within the lithium hydroxide layer [92].

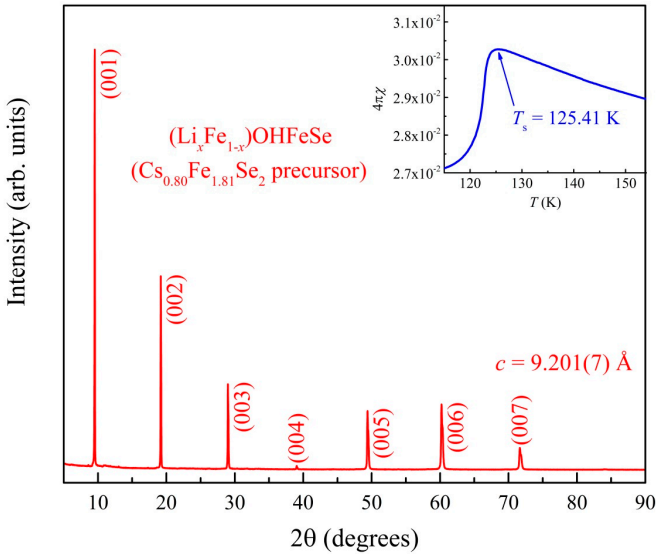

Figure 10. XRD patterns for the $(Li_{1-x}Fe_x)$OHFeSe single crystal which was synthesized at 180 °C for 72 h using the $Cs_{0.80}Fe_{1.81}Se_2$ precursor. The inset is the $4\pi\chi$–T curve, showing the antiferromagnetic (AFM) spin density wave (SDW) transition occurs at T_s = 125.41 K [53]. Reprinted with permission from IOP. All rights reserved.

5. Phase Diagram

The phase diagram of the $(Li_{1-x}Fe_x)$OHFeSe single crystals using the $A_{0.80}Fe_{1.81}Se_2$ (A = K, Rb, and Cs) crystal precursors is established based on c dependence of T_s and T_c, as shown in Figure 11. It can be seen that the crystals show AFM SDW and SC transitions in low and high c regions, respectively. As $T > T_s$ (T_c), Curie–Weiss (Pauli paramagnetic) phase forms. The phase diagram shows a step behavior of the AFM SDW and SC transitions between 9.254(3) and 9.255(1) Å, which is similar to that for polycrystalline samples of $LaO_{1-x}F_xFeAs$ [93], but different from those for cuprate SCs [94] and other FeSCs [95], such as $CeFeAsO_{1-x}F_x$, $(K,Tl)Fe_xSe_2$ [96], $NaFe_{1-x}Co_xAs$ [97], $Ba(Fe_{1-x}Co_x)_2As_2$, $SmFeAsO_{1-x}F_x$, $Ba_{1-x}K_xFe_2As_2$ [98], $BaFe_{2-x}Rh_xAs_2$, $BaFe_{2-x}Pd_xAs_2$, $SrFe_{2-x}Ni_xAs_2$, $SrFe_{2-x}Rh_xAs_2$, $SrFe_{2-x}Ir_xAs_2$, $SrFe_{2-x}Pd_xAs_2$. In addition, as c increases the T_c-c relationship experiences three regions successively: region 'I', region 'II', and region 'III'. In region 'I' ('II'), T_c gradually decreases (increases) stably as c increases. However, in region 'III', the T_c-c relationship is not stable, indicating that a large c-axis weakens the hydrogen bonding interaction between the layers which makes the structure and property unstable. The T_c-c relationship has a V-shape, which is in sharp contrast to the inverse V-shaped one in cuprate SCs [94] and other FeSCs [93,95–98]. The complex SC phase diagram can be attributed to the doping effect of the $(Li_{1-x}Fe_x)$OH layer (the Fe/Li ratio, the migration of Fe and the charge transfer from the intercalated layer to the FeSe layer) as well as the complex competing effects between the several different states related to phase separation [18,52,82,89,99–101]. Comparison of this phase diagram to that for $(Li_{1-x}Fe_x)$OHFeSe polycrystals shows some similarities [90]. They both have AFM SDW and SC phases, which lie in the low and high c regions, respectively. However, for the single crystals,

the AFM SDW phase exists in the region where $c \leq 9.254(3)$ Å, whereas for the polycrystals, the SC phase forms for $c \geq 9.2152(8)$ Å [90]. Therefore, in the region where 9.2152(8) Å $\leq c \leq$ 9.254(3) Å, the phase of the single crystal system differs from that of the polycrystalline system, even if both systems have the same c value. During the hydrothermal growth of $(Li_{1-x}Fe_x)$OHFeSe, the chemical reactions are different for synthesizing these two different kinds of samples: For the polycrystals it is a three-dimensional (3D)-diffusion-3D-growth process, but for growing the single crystals, it is a 2D-diffusion-1D-growth process, as shown in Figure 4. These different growth mechanisms, along with the size effect, are likely to lead to the significant differences in the characteristics observed between the two types of samples.

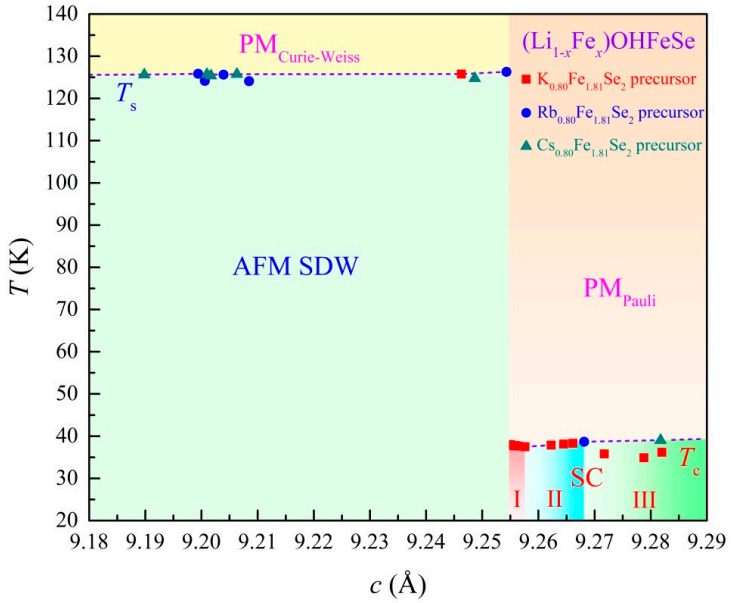

Figure 11. Phase diagram of $(Li_{1-x}Fe_x)$OHFeSe single crystals grown using $A_{0.80}Fe_{1.81}Se_2$ (A = K, Rb, and Cs) precursors. The values of T_s and T_c were derived from the $4\pi\chi$–T curves [53]. Reprinted with permission from IOP. All rights reserved.

6. Anisotropic Behavior

The anisotropic properties of a high-quality $(Li_{1-x}Fe_x)$OHFeSe single crystal have been systematically investigated by performing electrical and magnetic measurements [102].

Figure 12 shows the temperature dependence of the Hall coefficient R_H. It can be seen that R_H is negative in the whole temperature range from 2–300 K, indicating that electron-like charge carriers dominate in the crystal. R_H decreases as T decreases from room temperature, and reaches a minimum value at $T^* \approx 150$ K, below which it demonstrates a remarkable upturn. The strong temperature dependence of R_H may suggest a strong multiband-effect in the crystal: the electron scattering rate of each band varies with temperature differently, and thus a combined contribution of multiple bands may result in a strongly temperature dependent R_H. Another possible reason can be due to the magnetic skew scattering mechanism: scattering of conduction electrons from local moments is not symmetric because of spin-orbital coupling [103]. However, it is hard to distinguish between the different contributions from different mechanisms. A rough estimation based on the simple relation $R_H = -1/ne$ indicates that the carrier density n is low, i.e., n is estimated to be 3.0×10^{21} cm^{-3} at 225 K, which is similar to other anisotropic SCs, such as $NdFeAsO_{0.82}F_{0.18}$, polycrystalline $LaFeAsO_{0.9}F_{0.1-\delta}$, and cuprate SCs [103,104].

Figure 13 shows ρ_{ab}-T curves measured near T_c, where ρ_{ab} is the ab-plane resistivity. The onset T_c = 43 K and the residual resistance ratio RRR = ρ_{ab}(300 K)/ρ_{ab}(43 K) = 4.95. For both H || ab and H || c, T_c(0) decreases faster than T_c(onset) as $\mu_0 H$ increases, resulting in a broadening effect

of ΔT. Figure 13c shows that both $\Delta T(H \,||\, ab)$ and $\Delta T(H \,||\, c)$ increase monotonically with $\mu_0 H$. A quantitative fit gives $\Delta T \propto H^{\alpha}$, where α is a constant. For $H \,||\, ab$, α is 0.177 in the range of 0–9 T. For $H \,||\, c$, α is 0.076, 0.155, and 0.195 in region "I" ($\leq$1 T), region "II" (1–3 T), and region "III" (3–9 T), respectively. The broad SC transition at 0 T can be attributed to minority impurities, which are not observable in XRD measurements but may influence ΔT. Such minorities could be a normal state and/or SC phase. Furthermore, it can be seen that $\Delta T(H \,||\, c)$ is always larger than $\Delta T(H \,||\, ab)$, indicating that the broadening effect is anisotropic. The anisotropy ratio of ΔT is defined as $\eta = \Delta T(H \,||\, c)/\Delta T(H \,||\, ab)$. Figure 13c shows that in region "I", η increases rapidly with $\mu_0 H$. In region "II", the increase of η is very slow, and the maximum value $\eta_{max} = 1.67$ is obtained at 3 T. In region "III", η decreases steadily as $\mu_0 H$ increases, and $\eta = 1.64$ is reached at 9 T, showing that high fields can suppress the anisotropy ratio. The tunability of η as a function of $\mu_0 H$ shows great potential toward practical applications like magnetic sensors and switching devices.

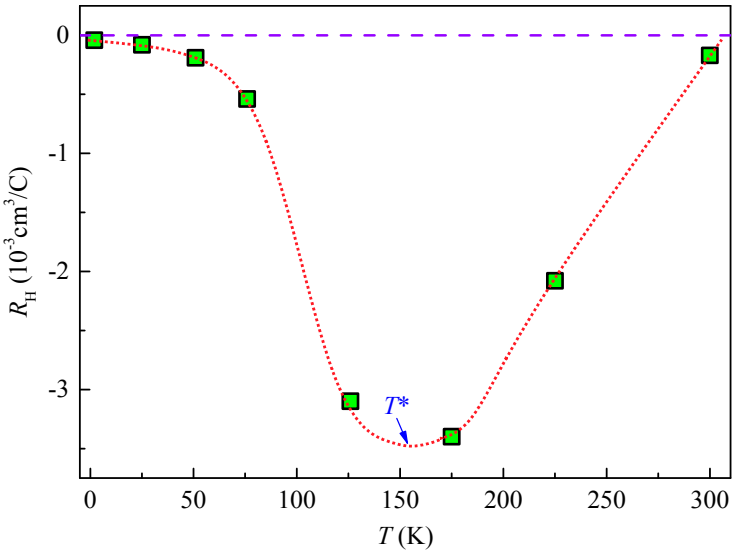

Figure 12. Temperature-dependent R_H of single-crystal $(Li_{1-x}Fe_x)OHFeSe$. The point-dashed curve is a guide for the eyes.

The broadening behavior of ΔT can be analyzed based on the thermally activated flux flow (TAFF) model, and the TA resistivity $\rho(T,H) = \rho_0 \exp(-U/T)$, where ρ_0 is a constant and U is the activation energy [105]. Assuming $U = U_0(1 - t)$, where $t = T/T_c$ is the reduced temperature and U_0 is apparent activation energy, the Arrhenius relation can be derived as $\ln\rho(T, H) = \ln\rho_0 + U_0/T_c - U_0/T$. Figure 14a,b show that the experimental data can be fitted very well using the Arrhenius relation (solid lines). Figure 14c shows the $\mu_0 H$ dependence of U_0. Inset of Figure 14c displays the same data on a double-logarithmic scale. It is seen that U_0 for $H \,||\, ab$ is much higher than for $H \,||\, c$, indicating a much stronger flux pinning for $H \,||\, ab$. In addition, for both configurations, it is found that U_0 decreases with increasing $\mu_0 H$ according to the power law of $U_0 \propto (1/H)^{\alpha}$, where α is a constant. In region "I" ($\leq$1 T) and region "II" (1–9 T), $\alpha = 0.364$ (0.615) and 0.645 (0.436) for $H \,||\, ab$ ($H \,||\, c$), respectively. For $H \,||\, ab$, the weak power-law decrease of U_0 in region "I" suggests that single-vortex pinning is dominant in low-field, while a more rapidly decrease of U_0 in region "II" can be related to the crossover to a collective pinning regime in high-field. However, it is reversed for $H \,||\, c$, suggesting that in region "I" ("II") collective (single-vortex) pinning is dominant. Furthermore, it can be seen that the anisotropy ratio $\sigma = U_0(H \,||\, ab)/U_0(H \,||\, c)$ also shows a crossover at 1 T. In region "I", σ increases rapidly with $\mu_0 H$, from $\sigma = 3.91$ at 0.25 T to the maximum value $\sigma_{max} = 5.53$ at 1 T. However, in region "II", σ decreases slowly as $\mu_0 H$ increases, to a minimum value $\sigma_{min} = 3.52$ at 9 T, indicating that high field weakens the anisotropy. In addition, σ is higher than that for a $Bi_{2.2}Sr_2Ca_{0.8}Cu_2O_{8+\delta}$

single crystal, which typically lies in the range of 1.5–3 [105]. Since σ can be tuned by the applied field, it shows great potential for device applications, such as in the development of magnetic field and temperature sensors.

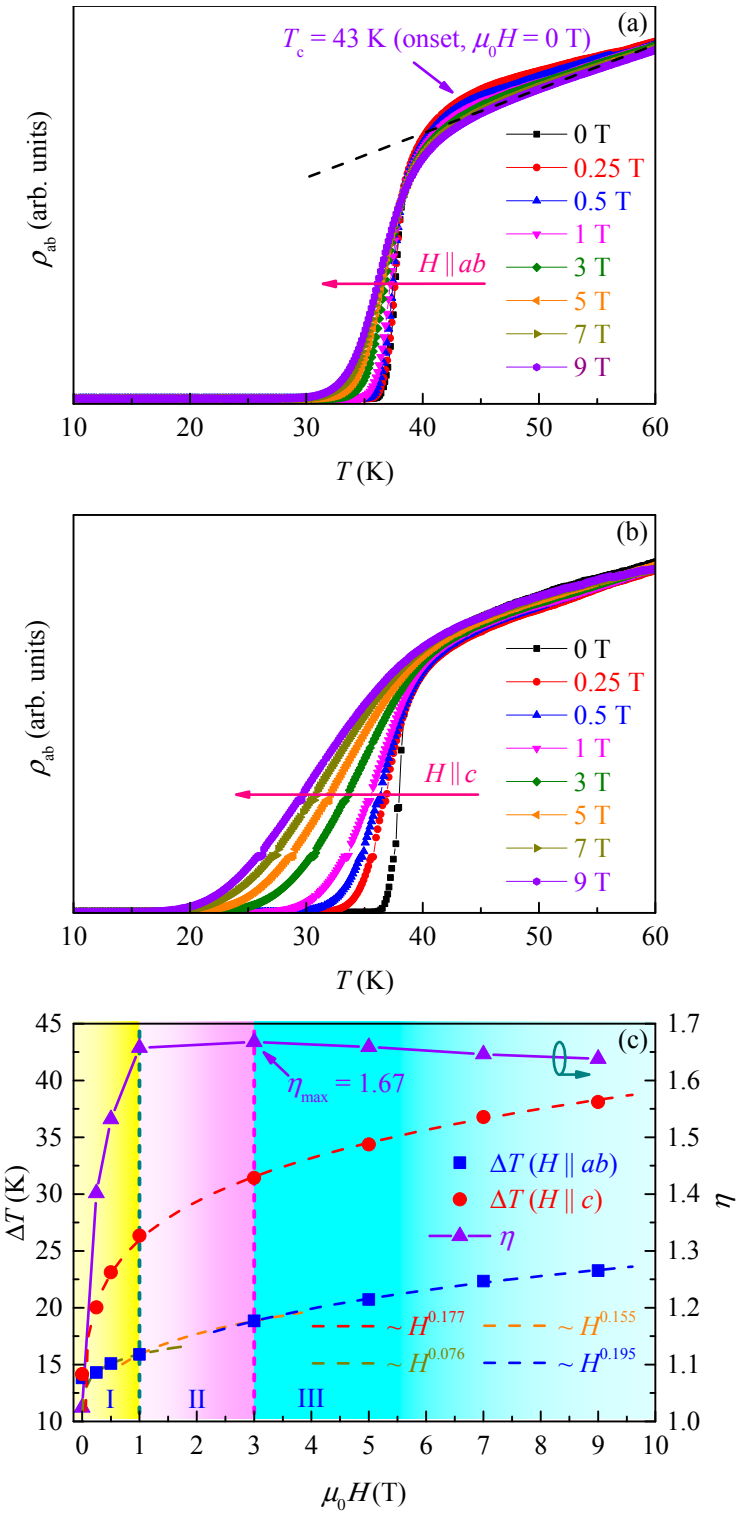

Figure 13. ρ_{ab}-T relations for (**a**) H | | ab and (**b**) H | | c. (**c**) ΔT-$\mu_0 H$ and η-$\mu_0 H$ relations. η_{max} = 1.67 at $\mu_0 H$ = 3 T.

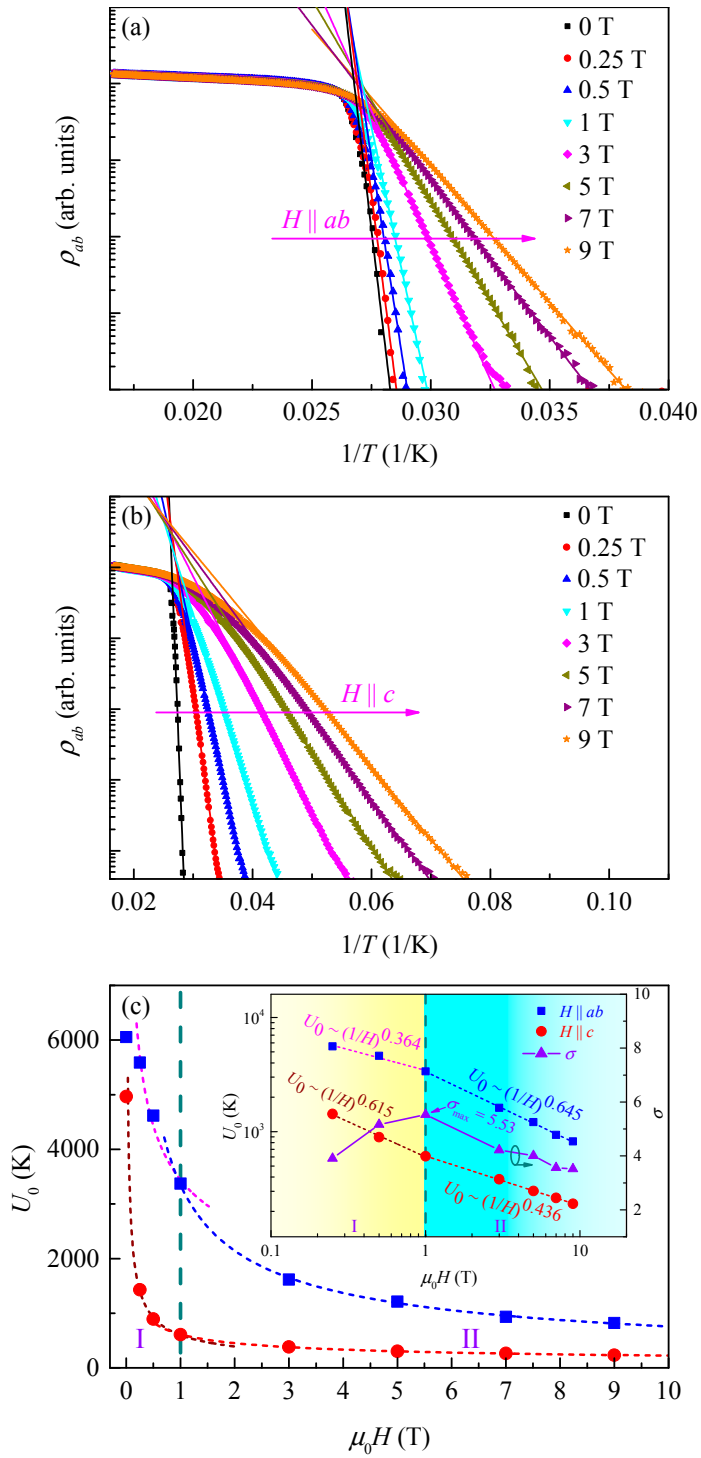

Figure 14. Arrhenius plot of ρ_{ab} for (**a**) H | | ab and (**b**) H | | c. (**c**) $\mu_0 H$ dependence of U_0 and σ. Inset of (**c**) shows the same data on a double-logarithmic scale.

Figure 15a shows temperature dependence of $\mu_0 H_{c2}$, where $\mu_0 H_{c2}$ is determined from the 10% and 50% criteria of the normal resistivity at the onset temperature. For both configurations, the curves show an upward curvature and the values of $d(\mu_0 H_{c2}^{\|ab})/dT$ and $d(\mu_0 H_{c2}^{\|c})/dT$ are calculated to be -12.30 (-4.01) and -1.61 (-1.27) T/K under the 50% (10%) criterion, respectively. For both criteria, the more positive curvature leads to much higher $\mu_0 H_{c2}$ for H | | ab than for H | | c. It is observed that in some FeSCs, $\mu_0 H_{c2}$ depends linearly on T due to the orbital limiting effect [106]. Based on

this, using linear extrapolation (LE), under the 50% (10%) criterion, the zero-temperature $\mu_0 H_{c2}$, $\mu_0 H_{c2}(0)$, is estimated to be 457.66 (144.74) T and 57.55 (39.17) T for H | | ab and H | | c, respectively, as shown in Figure 15b. The anisotropic ratio $\gamma = H_{c2}^{\|ab}(0)/H_{c2}^{\|c}(0) = 7.95$ (3.70) is obtained for the 50% (10%) criterion. In addition, $\mu_0 H_{c2}(0)$ can also be estimated using the Werthamer-Helfand-Hohenberg (WHH) equation $\mu_0 H_{c2}(0) = -0.693 T_c [d(\mu_0 H_{c2})/dT]_{T=T_c}$ [107]. For the 50% (10%) criterion, $\mu_0 H_{c2}(0) = 324.28$ (102.84) T and 42.45 (32.77) T are obtained from the WHH equation for H | | ab and H | | c, respectively, and thus $\gamma = 7.64$ (3.14) is obtained for the 50% (10%) criterion. The values of $\mu_0 H_{c2}(0)$ and γ obtained by the WHH model are all smaller than by the LE method. Based on the WHH theory and using the parameter values under the 50% criterion, the zero-temperature coherence lengths $\xi_{ab}(0)$ and $\xi_c(0)$ are estimated to be 2.7858 nm and 0.3647 nm, respectively, from Ginzburg-Landau theory. Furthermore, using $\gamma = (m_c/m_{ab})^{1/2}$, a value of $m_c/m_{ab} = 2.76$ is obtained, where m_c and m_{ab} are the effective mass tensors when the electrons are moving perpendicular and parallel to the FeSe layers, respectively.

The magnetization hysteresis loops of the crystal indicated anisotropic behavior and type-II superconductivity, as shown in Figure 16. The critical current density $J_c^{ab}(J_c^c)$ for H | | c (H | | ab) can be calculated using the extended Bean model [108]. Figure 17a,b show that for a given T ($\mu_0 H$), as $\mu_0 H$ (T) increases both J_c^{ab} and J_c^c decrease. When $T \leq 5$ K, J_c^{ab} (J_c^c) exceeds 1.44×10^4 (8.29×10^3) A/cm^2 in high fields up to 4 T. Figure 17c shows the temperature dependence of zero-field J_c, whose values are extracted by extrapolation to 0 T. J_c^{ab} is higher than J_c^c for a given T. The anisotropic ratio $\delta = J_c^{ab}/J_c^c$ increases from 2.90 to the maximum value of 3.48 as T increases from 2–7 K, but decreases as T increases further, and reaches its lowest value of 2.62 at 30 K. These results show that δ can be adjusted by varying temperature, providing a new basis for designing power-control or power-switching devices.

In order to study the vortex pinning mechanism, the authors plot the normalized pinning force $f_p = F_p/F_p^{max}$ as a function of the reduced field $h = H/H_{irr}$, where the pinning force density $F_p = \mu_0 H J_c$ and the irreversibility field $\mu_0 H_{irr}$ is obtained by extrapolating the $J_c{}^{1/2}(\mu_0 H)^{1/4}$ versus $\mu_0 H$ curve to the horizontal axis [109]. Values of $\mu_0 H_{irr} = 20.39$ T and 5.19 T are obtained for H | | ab and H | | c, respectively. The anisotropy of $\mu_0 H_{irr}$ is 20.39/5.19 = 3.93. Figure 18 shows that the formula $f_p \propto h^p(1-h)^q$ fits the experimental data well for each configuration at 15 K. Flux-pinning parameters of $p = 0.686$ (0.365) and $q = 3.242$ (2.452) are obtained for H | | ab (H | | c) by fitting. The position of the maximum of F_p/F_p^{max} is $h_{max} \approx p/(p+q)$. For H | | ab (H | | c), the fitting value $h_{max}^{fit} = 0.175$ (0.130) is consistent with the peak position $h_{max}^{exp} = 0.174$ (0.129) of the experimental curve. These values are close to $h_{max} = 0.2$ responsible for normal surface pinning (NSP) [110], indicating that the NSP mechanism is dominant in the crystal for each configuration. The ratio 0.175/0.130 = 1.35 shows a small anisotropy between the two orientations. However, for the quenched $K_xFe_{2-y}Se_2$ single crystals $h_{max} = 0.32$ or 0.34, indicating that the normal point pinning (NPP) is dominant [111,112]. For the Mn doped $K_xFe_{2-y}Se_2$ single crystal $h_{max} = 0.27$ is smaller than for the $K_xFe_{2-y}Se_2$ quenched crystals, implying that the NPP may coexist with NSP [112]. In the Mn doped $K_xFe_{2-y}Se_2$ single crystals, Mn atoms can form non-SC K-Fe-Mn inclusion phases, and such large normal inclusions may serve as the NSP centers in the crystals [112]. In comparison with the quenched and the Mn doped $K_xFe_{2-y}Se_2$ single crystals, h_{max} for the $(Li_{1-x}Fe_x)$OHFeSe single crystal is much smaller, indicating that the hydrothermal ion-exchange process is more effective for obtaining NSP centers and changing the pinning mechanism.

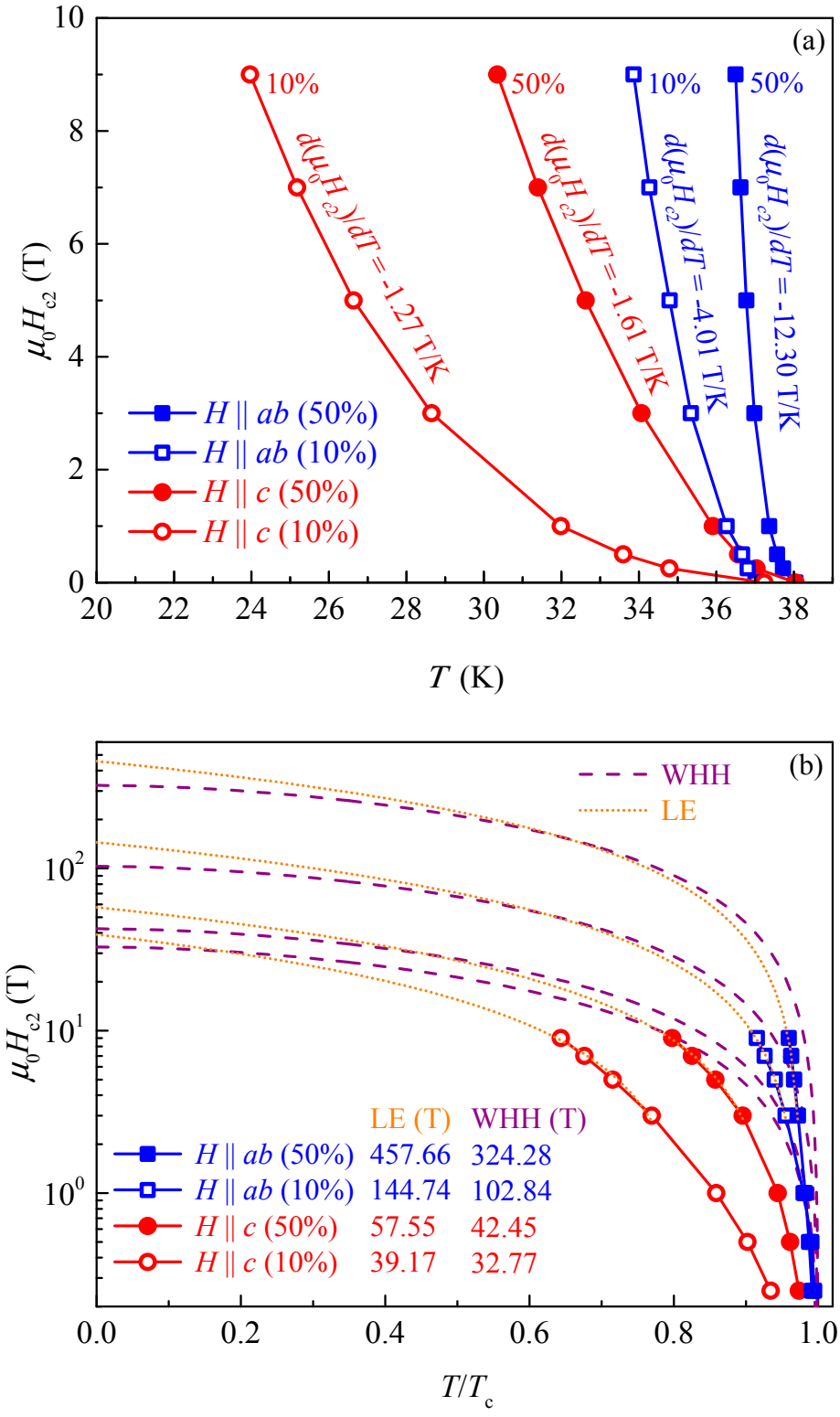

Figure 15. (**a**) $\mu_0 H_{c2}$-T relations; (**b**) the zero-temperature upper critical fields are extrapolated using Werthamer-Helfand-Hohenberg (WHH) formula and linear extrapolation (LE) method.

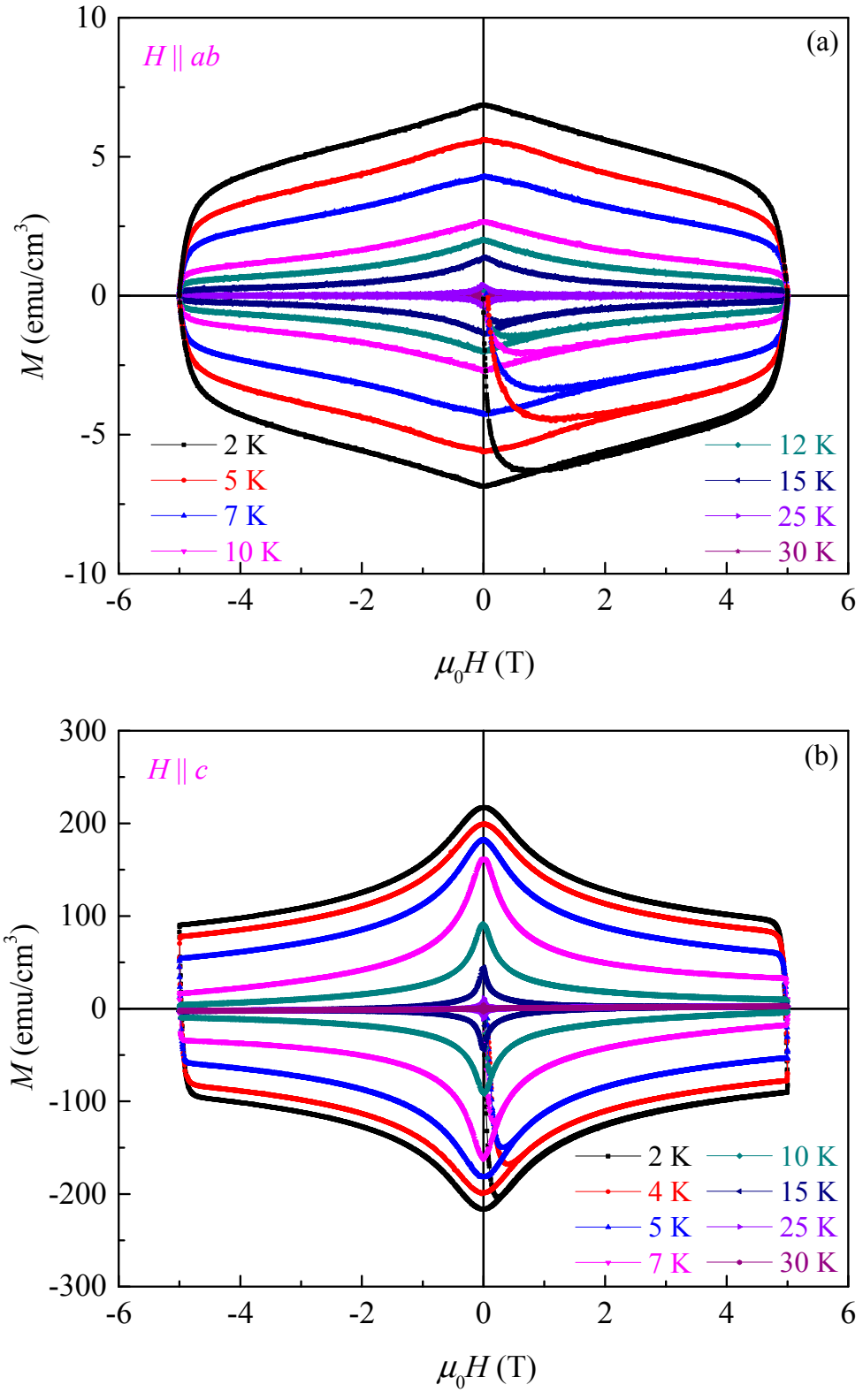

Figure 16. Magnetization hysteresis loops for (**a**) $H \mid\mid ab$ and (**b**) $H \mid\mid c$.

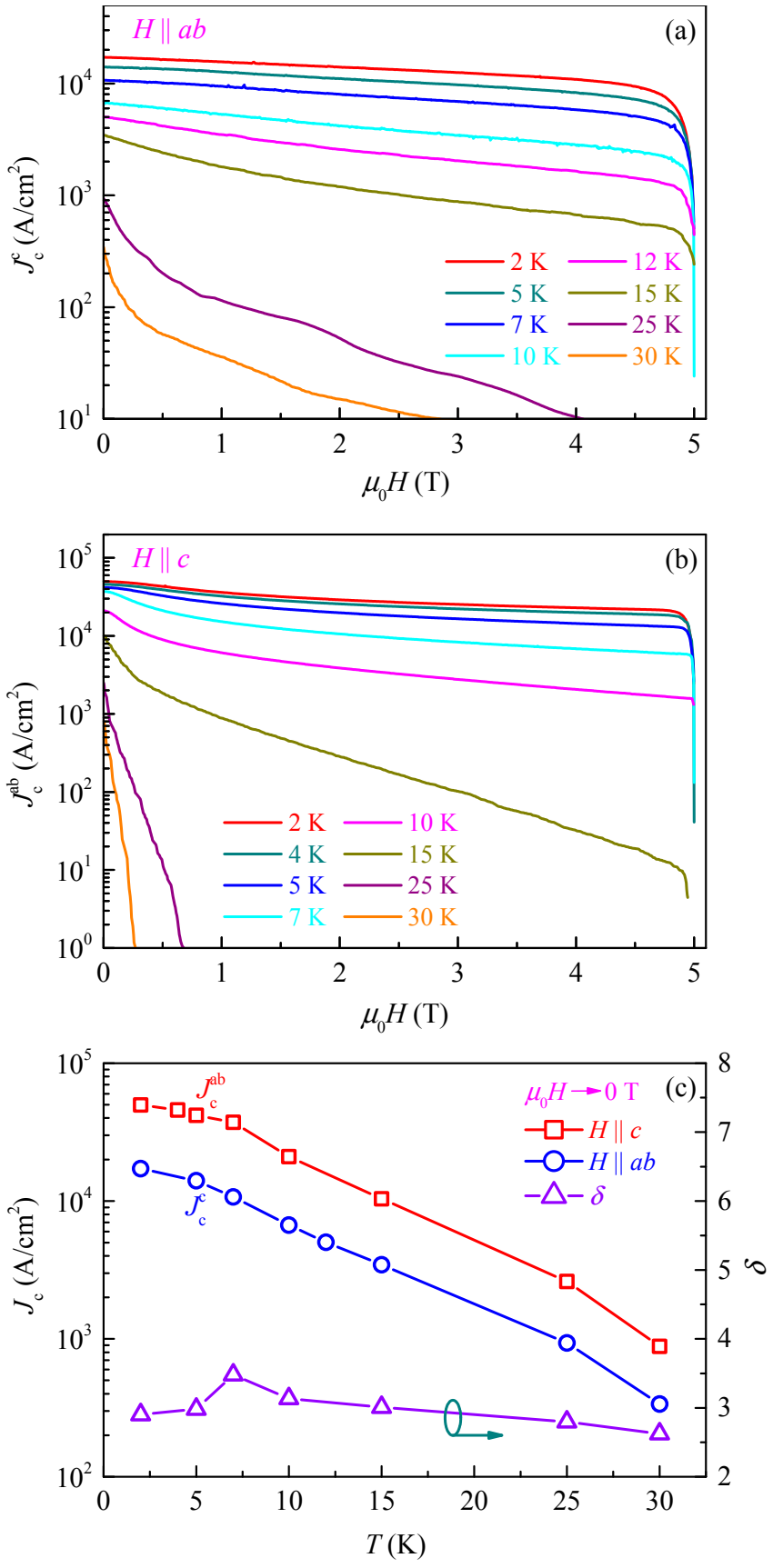

Figure 17. $\mu_0 H$ dependence of (**a**) J_c^c and (**b**) J_c^{ab} at different temperatures; (**c**) J_c-T and δ-T relations in the temperature range 2–30 K, $2.62 \leq \delta \leq 3.48$.

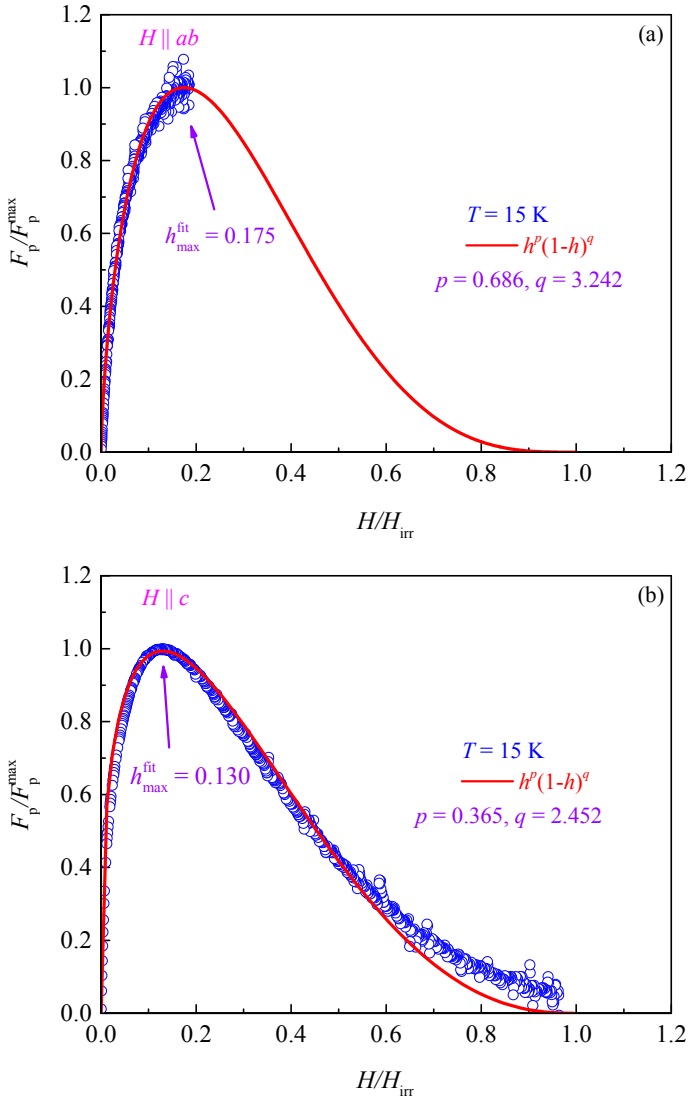

Figure 18. F_p/F_p^{max} as a function of $h = H/H_{irr}$ for (**a**) H | | ab and (**b**) H | | c. The solid curves are fits of the data to the formula $F_p/F_p^{max} \propto h^p(1-h)^q$.

7. Superconducting Mechanism

Density functional theory (DFT) calculations were used to investigate the dominant roles of the $(Li_{0.8}Fe_{0.2})$OH layers in the high-T_c superconductivity of $(Li_{0.8}Fe_{0.2})$OHFeSe, and it was found that substitution of Li by Fe can enhance the structural stability both in the ab plane and along the c axis. The Fe0.2 atoms can be the origin of significant electron injection into FeSe. The $(Li_{0.8}Fe_{0.2})$OH layers can be either AFM or FM depending on the spatial distribution of Fe0.2 atoms. The stable structure with large electron injection leads to high-T_c superconductivity [113]. In addition, low temperature scanning tunneling microscopy (STM) suggests that the $(Li_{1-x}Fe_x)$OHFeSe is a plain s-wave superconductor with strong coupling mechanism [114,115].

8. Conclusions

FeSCs have been attracting a great deal of research interest for the development of new high-T_c SCs. Their diverse structures, complex phases, and exotic SC properties are important for both fundamental studies and technical applications. In general, T_c can be enhanced by chemical and physical methods, such as ion doping and the application of external pressure. In addition, many measures have also been

taken to improve other SC properties in FeSC systems. In this paper, a hydrothermal method which can be used for inducing intercalation to increase T_c and improve other SC properties is reviewed, taking the $(Li_{1-x}Fe_x)$OHFeSe single crystal system as an example.

The hydrothermal method has been successfully applied to grow high-quality $(Li_{1-x}Fe_x)$OHFeSe single crystals using OFZ-grown $A_xFe_{2-y}Se_2$ (A = K, Rb, and Cs) precursors. A stacking layer of $(Li_{1-x}Fe_x)$OH sandwiched between the FeSe layers is formed by the hydrothermal ion exchange of Li/Fe–O–H for K, Rb, and Cs. The structure of the ion-exchanged crystal belongs to the $P4/nmm$ space group, which is different from the $I4/m$ space group of the $A_xFe_{2-y}Se_2$ precursor. In the $(Li_{1-x}Fe_x)$OHFeSe single crystals the space between two adjacent FeSe layers is enlarged by the intercalated $(Li_{1-x}Fe_x)$OH layers, resulting in both larger c-axis lattice constants and a higher T_c by weakening the interlayer coupling, compared to FeSe materials. In addition, the T_c of $(Li_{1-x}Fe_x)$OHFeSe crystals increases from 29.31 K to 42.69 K and from 28.67 K to 44.66 K compared to the SC $K_{0.80}Fe_{1.81}Se_2$ and poor SC $Cs_{0.80}Fe_{1.81}Se_2$ crystal precursors, respectively. For the insulating $Rb_{0.80}Fe_{1.81}Se_2$ crystal precursor, a significant change from insulator to superconductor occurs after the ion-exchange process, and T_c = 43.87 K is obtained in the synthesized $(Li_{1-x}Fe_x)$OHFeSe crystal. The sharp transitions of resistivity at T_c ~ 42 K with 100% SC shielding ratio confirm the bulk superconductivity of the $(Li_{1-x}Fe_x)$OHFeSe single crystals.

By optimizing the growth parameters, such as time, temperature, and composition, SC $(Li_{1-x}Fe_x)$OHFeSe single crystals have been obtained, regardless of the SC phase of the precursor such as SC $K_{0.80}Fe_{1.81}Se_2$ (T_c = 29.31 K), non-SC $Rb_{0.80}Fe_{1.81}Se_2$, or poor-SC $Cs_{0.80}Fe_{1.81}Se_2$ (T_c = 28.67 K). Furthermore, by adjusting the growth parameters, non-SC $(Li_{1-x}Fe_x)$OHFeSe single crystals showing AFM SDW have also been synthesized regardless of the SC phase of the precursor. For SC crystals, T_c > 42 K is achieved. Anisotropic properties including magnetoresistance broadening, upper critical field, coherence length, activation energy, magnetization hysteresis loops, critical current density, irreversibility field, and flux pinning were systematically reviewed. Crystal anisotropies are tunable through adjustments in the external magnetic field and temperature. In non-SC crystals, the AFM SDW transition occurs at ~125 K. The phase diagram including AFM SDW, SC and paramagnetic phases was summarized using the reviewed data. The results show that the $(Li_{1-x}Fe_x)$OHFeSe single crystal system provides a new research platform for both fundamental research and device applications.

Acknowledgments: The authors thank Alexander Blair for his assistance in refining the language used throughout this review.

Conflicts of Interest: The authors declare no conflict of interest.

References

1. Johrendt, D. Structure–property relationships of iron arsenide superconductors. *J. Mater. Chem.* **2011**, *21*, 13726–13736. [CrossRef]
2. Chen, D.P.; Lin, C.T. The growth of 122 and 11 iron-based superconductor single crystals and the influence of doping. *Supercond. Sci. Technol.* **2014**, *27*, 103002. [CrossRef]
3. Guo, J.G.; Jin, S.F.; Wang, G.; Wang, S.C.; Zhu, K.X.; Zhou, T.T.; He, M.; Chen, X.L. Superconductivity in the iron selenide $K_xFe_2Se_2$ ($0 \leq x \leq 1.0$). *Phys. Rev. B* **2010**, *82*, 180520. [CrossRef]
4. Li, M.T.; Chen, L.; Feng, Z.J.; Deng, D.; Kang, B.J.; Cao, S.X.; Lin, C.T.; Zhang, J.C. Anisotropic characteristics and critical behaviors in Mn doped $K_{0.8}Fe_2Se_2$ single crystal. *Physica C* **2014**, *506*, 40–46. [CrossRef]
5. Friemel, G.; Liu, W.P.; Goremychkin, E.A.; Liu, Y.; Park, J.T.; Sobolev, O.; Lin, C.T.; Keimer, B.; Inosov, D.S. Conformity of spin fluctuations in alkali-metal iron selenide superconductors inferred from the observation of a magnetic resonant mode in $K_xFe_{2-y}Se_2$. *Europhys. Lett.* **2012**, *99*, 67004. [CrossRef]
6. Kamihara, Y.; Watanabe, T.; Hirano, M.; Hosono, H. Iron-based layered superconductor $La[O_{1-x}F_x]FeAs$ (x = 0.05–0.12) with T_c = 26 K. *J. Am. Chem. Soc.* **2008**, *130*, 3296–3297. [CrossRef] [PubMed]
7. Hsu, F.C.; Luo, J.Y.; Yeh, K.W.; Chen, T.K.; Huang, T.W.; Wu, P.M.; Lee, Y.C.; Huang, Y.L.; Chu, Y.Y.; Yan, D.C.; et al. Superconductivity in the PbO-type structure α-FeSe. *Proc. Natl. Acad. Sci. USA* **2008**, *105*, 14262–14264. [CrossRef] [PubMed]

8. Mizuguchi, Y.; Hara, Y.; Deguchi, K.; Tsuda, S.; Yamaguchi, T.; Takeda, K.; Kotegawa, H.; Tou, H.; Takano, Y. Anion height dependence of T_c for the Fe-based superconductor. *Supercond. Sci. Technol.* **2010**, *23*, 054013. [CrossRef]
9. Hirschfeld, P.J.; Korshunov, M.M.; Mazin, I.I. Gap symmetry and structure of Fe-based superconductors. *Rep. Prog. Phys.* **2011**, *74*, 124508. [CrossRef]
10. Hanaguri, T.; Niitaka, S.; Kuroki, K.; Takagi, H. Unconventional s-wave superconductivity in Fe(Se,Te). *Science* **2010**, *328*, 474–476. [CrossRef] [PubMed]
11. Gasparov, V.A.; Audouard, A.; Drigo, L.; Rodigin, A.I.; Lin, C.T.; Liu, W.P.; Zhang, M.; Wang, A.F.; Chen, X.H.; Jeevan, H.S.; et al. Upper critical magnetic field of $K_xFe_{2-y}Se_2$ and $Eu_{0.5}K_{0.5}Fe_2As_2$ single crystals. *Phys. Rev. B* **2013**, *87*, 094508. [CrossRef]
12. Rahlenbeck, M.; Sun, G.L.; Sun, D.L.; Lin, C.T.; Keimer, B.; Ulrich, C. Phonon anomalies in pure and underdoped $R_{1-x}K_xFe_2As_2$ (R = Ba, Sr) investigated by Raman light scattering. *Phys. Rev. B* **2009**, *80*, 064509. [CrossRef]
13. Inosov, D.S.; Leineweber, A.; Yang, X.; Park, J.T.; Christensen, N.B.; Dinnebier, R.; Sun, G.L.; Niedermayer, C.; Haug, D.; Stephens, P.W.; et al. Suppression of the structural phase transition and lattice softening in slightly underdoped $Ba_{1-x}K_xFe_2As_2$ with electronic phase separation. *Phys. Rev. B* **2009**, *79*, 224503. [CrossRef]
14. Park, J.T.; Inosov, D.S.; Niedermayer, C.; Sun, G.L.; Haug, D.; Christensen, N.B.; Dinnebier, R.; Boris, A.V.; Drew, A.J.; Schulz, L.; et al. Electronic phase separation in the slightly underdoped iron pnictide superconductor $Ba_{1-x}K_xFe_2As_2$. *Phys. Rev. Lett.* **2009**, *102*, 117006. [CrossRef] [PubMed]
15. Zabolotnyy, V.B.; Inosov, D.S.; Evtushinsky, D.V.; Koitzsch, A.; Kordyuk, A.A.; Sun, G.L.; Park, J.T.; Haug, D.; Hinkov, V.; Boris, A.V.; et al. (π, π) electronic order in iron arsenide superconductors. *Nature* **2009**, *457*, 569–572. [CrossRef] [PubMed]
16. Liu, Y.; Lin, C.T. A comparative study of $Fe_{1+\delta}Te_{1-x}Se_x$ single crystals grown by Bridgman and self-flux techniques. *J. Supercond. Nov. Magn.* **2011**, *24*, 183–187. [CrossRef]
17. Liu, R.H.; Wu, T.; Wu, G.; Chen, H.; Wang, X.F.; Xie, Y.L.; Yin, J.J.; Yan, Y.J.; Li, Q.J.; Shi, B.C.; et al. A large iron isotope effect in $SmFeAsO_{1-x}F_x$ and $Ba_{1-x}K_xFe_2As_2$. *Nature* **2009**, *459*, 64–67. [CrossRef] [PubMed]
18. Dagotto, E. *Colloquium*: The unexpected properties of alkali metal iron selenide superconductors. *Rev. Mod. Phys.* **2013**, *85*, 849–867. [CrossRef]
19. Büchner, B.; Hess, C. Iron-based superconductors: Vital clues from a basic compound. *Nat. Mater.* **2009**, *8*, 615–616. [CrossRef] [PubMed]
20. Tapp, J.H.; Tang, Z.; Lv, B.; Sasmal, K.; Lorenz, B.; Chu, P.C.W.; Guloy, A.M. LiFeAs: An intrinsic FeAs-based superconductor with T_c = 18 K. *Phys. Rev. B* **2008**, *78*, 060505. [CrossRef]
21. Wang, X.C.; Liu, Q.; Lv, Y.; Gao, W.; Yang, L.X.; Yu, R.C.; Li, F.Y.; Jin, C.Q. The superconductivity at 18 K in LiFeAs system. *Solid. State Commun.* **2008**, *148*, 538–540. [CrossRef]
22. Pitcher, M.J.; Parker, D.R.; Adamson, P.; Herkelrath, S.J.C.; Boothroyd, A.T.; Ibberson, R.M.; Brunelli, M.; Clarke, S.J. Structure and superconductivity of LiFeAs. *Chem. Commun.* **2008**, *45*, 5918–5920. [CrossRef] [PubMed]
23. Rotter, M.; Tegel, M.; Johrendt, D. Superconductivity at 38 K in the iron arsenide $(Ba_{1-x}K_x)Fe_2As_2$. *Phys. Rev. Lett.* **2008**, *101*, 107006. [CrossRef] [PubMed]
24. Sasmal, K.; Lv, B.; Lorenz, B.; Guloy, A.M.; Chen, F.; Xue, Y.Y.; Chu, C.W. Superconducting Fe-based compounds $(A_{1-x}Sr_x)Fe_2As_2$ with A = K and Cs with transition temperatures up to 37 K. *Phys. Rev. Lett.* **2008**, *101*, 107007. [CrossRef] [PubMed]
25. Chen, X.H.; Wu, T.; Wu, G.; Liu, R.H.; Chen, H.; Fang, D.F. Superconductivity at 43 K in $SmFeAsO_{1-x}F_x$. *Nature* **2008**, *453*, 761–762. [CrossRef] [PubMed]
26. Ren, Z.A.; Che, G.C.; Dong, X.L.; Yang, J.; Lu, W.; Yi, W.; Shen, X.L.; Li, Z.C.; Sun, L.L.; Zhou, F.; Zhao, Z.X. Superconductivity and phase diagram in iron-based arsenic-oxides $ReFeAsO_{1-\delta}$ (Re = rare-earth metal) without fluorine doping. *Europhys. Lett.* **2008**, *83*, 17002. [CrossRef]
27. Matsuishi, S.; Inoue, Y.; Nomura, T.; Yanagi, H.; Hirano, M.; Hosono, H. Superconductivity induced by Co-doping in quaternary fluoroarsenide CaFeAsF. *J. Am. Chem. Soc.* **2008**, *130*, 14428–14429. [CrossRef] [PubMed]
28. Ogino, H.; Matsumura, Y.; Katsura, Y.; Ushiyama, K.; Horii, S.; Kishio, K.; Shimoyama, J. Superconductivity at 17 K in $(Fe_2P_2)(Sr_4Sc_2O_6)$: A new superconducting layered pnictide oxide with a thick perovskite oxide layer. *Supercond. Sci. Technol.* **2009**, *22*, 075008. [CrossRef]

29. Zhu, X.Y.; Han, F.; Mu, G.; Cheng, P.; Shen, B.; Zeng, B.; Wen, H.H. Transition of stoichiometric Sr_2VO_3FeAs to a superconducting state at 37.2 K. *Phys. Rev. B* **2009**, *79*, 220512. [CrossRef]
30. Shirage, P.M.; Kihou, K.; Lee, C.H.; Kito, H.; Eisaki, H.; Lyo, A. Emergence of superconductivity in "32522" structure of $(Ca_3Al_2O_{5-y})(Fe_2Pn_2)$ (Pn = As and P). *J. Am. Chem. Soc.* **2011**, *133*, 9630–9633. [CrossRef] [PubMed]
31. Ren, Z.-A.; Lu, W.; Yang, J.; Yi, W.; Shen, X.-L.; Li, Z.-C.; Che, G.-C.; Dong, X.-L.; Sun, L.-L.; Zhou, F.; et al. Superconductivity at 55 K in iron-based F-doped layered quaternary compound $Sm[O_{1-x}F_x]FeAs$. *Chin. Phys. Lett.* **2008**, *25*, 2215–2216.
32. Wu, G.; Xie, Y.L.; Chen, H.; Zhong, M.; Liu, R.H.; Shi, B.C.; Li, Q.J.; Wang, X.F.; Wu, T.; Yan, Y.J.; et al. Superconductivity at 56 K in samarium-doped SrFeAsF. *J. Phys. Condens. Matter* **2009**, *21*, 142203. [CrossRef] [PubMed]
33. Chen, X.H.; Dai, P.C.; Feng, D.L.; Xiang, T.; Zhang, F.-C. Iron-based high transition temperature superconductors. *Natl. Sci. Rev.* **2014**, *1*, 371–395. [CrossRef]
34. Lei, H.; Wang, K.; Hu, R.; Ryu, H.; Abeykoon, M.; Bozin, E.S.; Petrovic, C. Iron chalcogenide superconductors at high magnetic fields. *Sci. Technol. Adv. Mater.* **2012**, *13*, 054305. [CrossRef] [PubMed]
35. Chen, T.-K.; Chang, C.-C.; Chang, H.-H.; Fang, A.-H.; Wang, C.-H.; Chao, W.-H.; Tseng, C.-M.; Lee, Y.-C.; Wu, Y.-R.; Wen, M.-H.; et al. Fe-vacancy order and superconductivity in tetragonal β-$Fe_{1-x}Se$. *Proc. Natl. Acad. Sci. USA* **2014**, *111*, 63–68. [CrossRef] [PubMed]
36. Yeh, K.-W.; Huang, T.-W.; Huang, Y.-L.; Chen, T.-K.; Hsu, F.-C.; Wu, P.M.; Lee, Y.-C.; Chu, Y.-Y.; Chen, C.-L.; Luo, J.-Y.; et al. Tellurium substitution effect on superconductivity of the α-phase iron selenide. *Europhys. Lett.* **2008**, *84*, 37002. [CrossRef]
37. Medvedev, S.; McQueen, T.M.; Troyan, I.A.; Palasyuk, T.; Eremets, M.I.; Cava, R.J.; Naghavi, S.; Casper, F.; Ksenofontov, V.; Wortmann, G.; et al. Electronic and magnetic phase diagram of bold italic β-$Fe_{1.01}Se$ with superconductivity at 36.7 K under pressure. *Nat. Mater.* **2009**, *8*, 630–633. [CrossRef] [PubMed]
38. Mizuguchi, Y.; Tomioka, F.; Tsuda, S.; Yamaguchi, T.; Takano, Y. Superconductivity at 27 K in tetragonal FeSe under high pressure. *Appl. Phys. Lett.* **2008**, *93*, 152505. [CrossRef]
39. Gati, E.; Köhler, S.; Guterding, D.; Wolf, B.; Knöner, S.; Ran, S.; Bud'ko, S.L.; Canfield, P.C.; Lang, M. Hydrostatic-pressure tuning of magnetic, nonmagnetic, and superconducting states in annealed $Ca(Fe_{1-x}Co_x)_2As_2$. *Phys. Rev. B* **2012**, *86*, 220511. [CrossRef]
40. Bao, W. Structure, magnetic order and excitations in the 245 family of Fe-based superconductors. *J. Phys. Condens. Matter* **2015**, *27*, 023201. [CrossRef] [PubMed]
41. Stewart, G.R. Superconductivity in iron compounds. *Rev. Mod. Phys.* **2011**, *83*, 1589–1652. [CrossRef]
42. Liu, R.H.; Luo, X.G.; Zhang, M.; Wang, A.F.; Ying, J.J.; Wang, X.F.; Yan, Y.J.; Xiang, Z.J.; Cheng, P.; Ye, G.J.; et al. Coexistence of superconductivity and antiferromagnetism in single crystals $A_{0.8}Fe_{2-y}Se_2$ (A=K, Rb, Cs, Tl/K and Tl/Rb): Evidence from magnetization and resistivity. *Europhys. Lett.* **2011**, *94*, 27008. [CrossRef]
43. Scheidt, E.-W.; Hathwar, V.R.; Schmitz, D.; Dunbar, A.; Scherer, W.; Mayr, F.; Tsurkan, V.; Deisenhofer, J.; Loidl, A. Superconductivity at T_c = 44 K in $Li_xFe_2Se_2$ $(NH_3)_y$. *Eur. Phys. J. B* **2012**, *85*, 279. [CrossRef]
44. Zheng, L.; Izumi, M.; Sakai, Y.; Eguchi, R.; Goto, H.; Takabayashi, Y.; Kambe, T.; Onji, T.; Araki, S.; Kobayashi, T.C.; et al. Superconductivity in $(NH_3)_yCs_{0.4}FeSe$. *Phys. Rev. B* **2013**, *88*, 094521. [CrossRef]
45. Burrard-Lucas, M.; Free, D.G.; Sedlmaier, S.J.; Wright, J.D.; Cassidy, S.J.; Hara, Y.; Corkett, A.J.; Lancaster, T.; Baker, P.J.; Blundell, S.J.; et al. Enhancement of the superconducting transition temperature of FeSe by intercalation of a molecular spacer layer. *Nat. Mater.* **2013**, *12*, 15. [CrossRef] [PubMed]
46. Krzton-Maziopa, A.; Pomjakushina, E.V.; Pomjakushin, V.Y.; von Rohr, F.; Schilling, A.; Conder, K. Synthesis of a new alkali meta–organic solvent intercalated iron selenide superconductor with $T_c \approx 45$ K. *J. Phys. Condens. Matter* **2012**, *24*, 382202. [CrossRef] [PubMed]
47. Ying, T.; Chen, X.; Wang, G.; Jin, S.; Lai, X.; Zhou, T.; Zhang, H.; Shen, S.; Wang, W. Superconducting phases in potassium-intercalated iron selenides. *J. Am. Chem. Soc.* **2013**, *135*, 2951–2954. [CrossRef] [PubMed]
48. Fang, M.H.; Pham, H.M.; Qian, B.; Liu, T.J.; Vehstedt, E.K.; Liu, Y.; Spinu, L.; Mao, Z.Q. Superconductivity close to magnetic instability in $Fe(Se_{1-x}Te_x)_{0.82}$. *Phys. Rev. B* **2008**, *78*, 224503. [CrossRef]
49. Long, Y.J.; Wang, D.M.; Wang, Z.; Yang, H.X.; He, J.B.; Zhao, L.X.; Wang, P.P.; Xue, M.Q.; Li, J.Q.; Ren, Z.A.; et al. Synthesis and characterization of the layered iron-selenide $Na_{0.8}Fe_{1.6}Se_2$. *Phys. Rev. B* **2014**, *90*, 144519. [CrossRef]

50. Ricci, A.; Poccia, N.; Joseph, B.; Innocenti, D.; Campi, G.; Zozulya, A.; Westermeier, F.; Schavkan, A.; Coneri, F.; Bianconi, A.; et al. Direct observation of nanoscale interface phase in the superconducting chalcogenide $K_xFe_{2-y}Se_2$ with intrinsic phase separation. *Phys. Rev. B* **2015**, *91*, 020503. [CrossRef]
51. Shoemaker, D.P.; Chung, D.Y.; Claus, H.; Francisco, M.C.; Avci, S.; Llobet, A.; Kanatzidis, M.G. Phase relations in $K_xFe_{2-y}Se_2$ and the structure of superconducting $K_xFe_2Se_2$ via high-resolution synchrotron diffraction. *Phys. Rev. B* **2012**, *86*, 184511. [CrossRef]
52. Lu, X.F.; Wang, N.Z.; Wu, H.; Wu, Y.P.; Zhao, D.; Zeng, X.Z.; Luo, X.G.; Wu, T.; Bao, W.; Zhang, G.H.; et al. Coexistence of superconductivity and antiferromagnetism in $(Li_{0.8}Fe_{0.2})$OHFeSe. *Nat. Mater.* **2015**, *14*, 325–329. [CrossRef] [PubMed]
53. Yu, G.; Zhang, G.Y.; Ryu, G.H.; Lin, C.T. Structure and superconductivity of $(Li_{1-x}Fe_x)$OHFeSe single crystals grown using $A_xFe_{2-y}Se_2$ (A = K, Rb, and Cs) as precursors. *J. Phys. Condens. Matter* **2016**, *28*, 015701. [CrossRef] [PubMed]
54. Liu, Y.; Xing, Q.; Dennis, K.W.; McCallum, R.W.; Lograsso, T.A. Evolution of precipitate morphology during heat treatment and its implications for the superconductivity in $K_xFe_{1.6+y}Se_2$ single crystals. *Phys. Rev. B* **2012**, *86*, 144507. [CrossRef]
55. Mizuguchi, Y.; Takeya, H.; Kawasaki, Y.; Ozaki, T.; Tsuda, S.; Yamaguchi, T.; Takano, Y. Transport properties of the new Fe-based superconductor $K_xFe_2Se_2$ (T_c = 33 K). *Appl. Phys. Lett.* **2011**, *98*, 042511. [CrossRef]
56. Ying, J.J.; Wang, X.F.; Luo, X.G.; Wang, A.F.; Zhang, M.; Yan, Y.J.; Xiang, Z.J.; Liu, R.H.; Cheng, P.; Ye, G.J.; et al. Superconductivity and magnetic properties of single crystals of $K_{0.75}Fe_{1.66}Se_2$ and $Cs_{0.81}Fe_{1.61}Se_2$. *Phys. Rev. B* **2011**, *83*, 212502. [CrossRef]
57. Wang, A.F.; Ying, J.J.; Yan, Y.J.; Liu, R.H.; Luo, X.G.; Li, Z.Y.; Wang, X.F.; Zhang, M.; Ye, G.J.; Cheng, P.; et al. Superconductivity at 32 K in single-crystalline $Rb_xFe_{2-y}Se_2$. *Phys. Rev. B* **2011**, *83*, 060512. [CrossRef]
58. Krzton-Maziopa, A.; Shermadini, Z.; Pomjakushina, E.; Pomjakushin, V.; Bendele, M.; Amato, A.; Khasanov, R.; Luetkens, H.; Conder, K. Synthesis and crystal growth of $Cs_{0.8}(FeSe_{0.98})_2$: A new iron-based superconductor with T_c = 27 K. *J. Phys. Condens. Matter* **2011**, *23*, 052203. [CrossRef] [PubMed]
59. Hu, R.; Cho, K.; Kim, H.; Hodovanets, H.; Straszheim, W.E.; Tanatar, M.A.; Prozorov, R.; Bud'ko, S.L.; Canfield, P.C. Anisotropic magnetism, resistivity, London penetration depth and magneto-optical imaging of superconducting $K_{0.80}Fe_{1.76}Se_2$ single crystals. *Supercond. Sci. Technol.* **2011**, *24*, 065006. [CrossRef]
60. Luo, X.G.; Wang, X.F.; Ying, J.J.; Yan, Y.J.; Li, Z.Y.; Zhang, M.; Wang, A.F.; Cheng, P.; Xiang, Z.J.; Ye, G.J.; et al. Crystal structure, physical properties and superconductivity in $A_xFe_2Se_2$ single crystals. *New J. Phys.* **2011**, *13*, 053011. [CrossRef]
61. Wang, D.M.; He, J.B.; Xia, T.-L.; Chen, G.F. Effect of varying iron content on the transport properties of the potassium-intercalated iron selenide $K_xFe_{2-y}Se_2$. *Phys. Rev. B* **2011**, *83*, 132502. [CrossRef]
62. Tsurkan, V.; Deisenhofer, J.; Günther, A.; Krug von Nidder, H.-A.; Widmann, S.; Loidl, A. Anisotropic magnetism, superconductivity and the phase diagram of $Rb_{1-x}Fe_{2-y}Se_2$. *Phys. Rev. B* **2011**, *84*, 144520. [CrossRef]
63. Liu, Y.; Li, Z.C.; Liu, W.P.; Friemel, G.; Inosov, D.S.; Dinnebier, R.E.; Li, Z.J.; Lin, C.T. $K_xFe_{2-y}Se_2$ single crystals: Floating-zone growth, transport and structural properties. *Supercond. Sci. Technol.* **2012**, *25*, 075001. [CrossRef]
64. Maljuk, A.; Watauchi, S.; Tanakab, I.; Kojima, H. The effect of B_2O_3 addition on $La_{2-x}Sr_xCuO_4$ single-crystal growth. *J. Cryst. Growth* **2000**, *212*, 138–141. [CrossRef]
65. Lin, C.T.; Maljuk, A.; Liang, B. The seeding effect of floating zone growth on $Nd_{1.85}Ce_{0.15}CuO_4$ and $Bi_2Sr_2CaCu_2O_{8-\delta}$ single crystals. *Supercond. Sci. Technol.* **2002**, *15*, 1736–1740. [CrossRef]
66. Liang, B.; Lin, C.T. On the growth of underdoped $Bi_2Sr_2CaCu_2O_{8+\delta}$ single crystals by traveling solvent floating zone method. *J. Cryst. Growth* **2002**, *237*, 756–761. [CrossRef]
67. Maljuk, A.; Liang, B.; Lin, C.T.; Emelchenko, G.A. On the growth of overdoped Bi-2212 single crystals under high oxygen pressure. *Physica C* **2001**, *355*, 140–146. [CrossRef]
68. Gu, G.D.; Takamuku, K.; Koshizuka, N.; Tanaka, S. Large single crystal Bi-2212 along the c-axis prepared by floating zone method. *J. Cryst. Growth* **1993**, *130*, 325–329. [CrossRef]
69. Lin, C.T.; Freiberg, M.; Schöenherr, E. Growth and oxygenating studies of $Bi_{2+x}Sr_{2-x}Ca_{n-1}Cu_nO_{2n+4+\delta}$ single crystals. *Physica C* **2000**, *337*, 270–276. [CrossRef]
70. Takekawa, S.; Nozaki, H.; Umezono, A.; Kosuda, K.; Kobayashi, M. Single crystal growth of the superconductor $Bi_{2.0}(Bi_{0.2}Sr_{1.8}Ca_{1.0})Cu_{2.0}O_8$. *J. Cryst. Growth* **1988**, *92*, 687–690. [CrossRef]

71. Gu, G.D.; Lin, Z.W. Single crystal growth of high-temperature superconductor $Bi_{2.1}Sr_{1.9}Ca_{1.0}Cu_{2.0}Al_yO_x$. *Supercond. Sci. Technol.* **2000**, *13*, 1197–1201. [CrossRef]
72. Maljuk, A.; Lin, C.T. Floating zone growth of $Bi_2Sr_2Ca_2Cu_3O_y$ superconductor. *Crystals* **2016**, *6*, 62. [CrossRef]
73. Liang, B.; Lin, C.T.; Shang, P.; Yang, G. Single crystals of triple-layered cuprates $Bi_2Sr_2Ca_2Cu_3O_{10+\delta}$: Growth, annealing and characterization. *Physica C* **2002**, *383*, 75–88. [CrossRef]
74. Kulakov, A.B.; Maier, D.; Maljuk, A.; Bdikin, I.K.; Lin, C.T. Study of growth/intergrowth behavior and structural analyses of $Bi_2Sr_2Ca_2Cu_3O_{10+\delta}$ single crystals. *J. Cryst. Growth* **2006**, *296*, 69–74. [CrossRef]
75. Fujii, T.; Watanabe, T.; Matsuda, A. Single-crystal growth of $Bi_2Sr_2Ca_2Cu_3O_{10+\delta}$ (Bi-2223) by TSFZ method. *J. Cryst. Growth* **2001**, *223*, 175–180. [CrossRef]
76. Peng, F.; Liu, W.P.; Lin, C.T. Study of thermal behavior and single crystal growth of $A_{0.8}Fe_{1.81}Se_2$ (A = K, Rb, and, Cs). *J. Supercond. Nov. Magn.* **2013**, *26*, 1205–1211. [CrossRef]
77. Liu, W.P.; Li, M.T.; Lin, C.T. Effect of Te doping on the structure and superconductivity of $K_xFe_{2-y}Se_{2-z}Te_z$ single crystals. *J. Supercond. Nov. Magn.* **2014**, *27*, 2419–2426. [CrossRef]
78. McMillen, C.D.; Kolis, J.W. Bulk single crystal growth from hydrothermal solutions. *Philos. Mag.* **2012**, *92*, 2686–2711. [CrossRef]
79. Zhang, G.; Li, G.; Huang, F.; Liao, F.; Li, K.; Wang, Y.; Lin, J. Hydrothermal synthesis of superconductors $Ba_{1-x}K_xBiO_3$ and double perovskites $Ba_{1-x}K_xBi_{1-y}Na_yO_3$. *J. Alloys Compd.* **2011**, *509*, 9804–9808. [CrossRef]
80. Hirano, S.; Takahashi, S. Hydrothermal synthesis and properties of $BaPb_{1-x}Bi_xO_3$. *J. Cryst. Growth* **1986**, *79*, 219–222. [CrossRef]
81. Lan, Y.C.; Chen, X.L.; Cao, Y.G.; Huang, J.K.; Che, G.C.; Liu, G.D.; Xu, Y.P.; Xu, T.; Li, J.Y. Structure and superconducting properties of chemically oxidized La_2CuO_{4+y} under hydrothermal conditions. *Physica C* **2000**, *336*, 151–156. [CrossRef]
82. Sun, H.; Woodru, D.N.; Cassidy, S.J.; Allcroft, G.M.; Sedlmaier, S.J.; Thompson, A.L.; Bingham, P.A.; Forder, S.D.; Cartenet, S.; Mary, N.; et al. Soft Chemical control of superconductivity in lithium iron selenide hydroxides $Li_{1-x}Fe_x(OH)Fe_{1-y}Se$. *Inorg. Chem.* **2015**, *54*, 1958–1964. [CrossRef] [PubMed]
83. Pachmayr, U.; Nitsche, F.; Luetkens, H.; Kamusella, S.; Brückner, F.; Sarkar, R.; Klauss, H.-H.; Johrendt, D. Coexistence of 3d-ferromagnetism and superconductivity in $[(Li_{1-x}Fe_x)OH](Fe_{1-y}Li_y)Se$. *Angew. Chem. Int. Ed. Engl.* **2015**, *54*, 293–297. [CrossRef] [PubMed]
84. Shermadini, Z.; Luetkens, H.; Khasanov, R.; Krzton-Maziopa, A.; Conder, K.; Pomjakushina, E.; Klauss, H.-H.; Amato, A. Superconducting properties of single-crystalline $A_xFe_{2-y}Se_2$ (A=Rb, K) studied using muon spin spectroscopy. *Phys. Rev. B* **2012**, *85*, 100501. [CrossRef]
85. Lynn, J.W.; Zhou, X.; Borg, C.K.H.; Saha, S.R.; Paglione, J.; Rodriguez, E.E. Neutron investigation of the magnetic scattering in an iron-based ferromagnetic superconductor. *Phys. Rev. B* **2015**, *92*, 060510. [CrossRef]
86. Nejasattari, F.; Stadnik, Z.M. Search for Fe magnetic ordering in the 40 K superconductor $(Li_{0.8}Fe_{0.2})$OHFeSe. *J. Alloy Compd.* **2015**, *652*, 470. [CrossRef]
87. McQueen, T.M.; Huang, Q.; Ksenofontov, V.; Felser, C.; Xu, Q.; Zandbergen, H.; Hor, Y.S.; Allred, J.; Williams, A.J.; Qu, D.; et al. Extreme sensitivity of superconductivity to stoichiometry in $Fe_{1+\delta}Se$. *Phys. Rev. B* **2009**, *79*, 014522. [CrossRef]
88. Sun, Y.; Park, A.; Pyon, S.; Tamegai, T.; Kambara, T.; Ichinose, A. Effects of heavy-ion irradiation on FeSe. *Phys. Rev. B* **2017**, *95*, 104514. [CrossRef]
89. Ying, J.J.; Wang, X.F.; Luo, X.G.; Li, Z.Y.; Yan, Y.J.; Zhang, M.; Wang, A.F.; Cheng, P.; Ye, G.J.; Xiang, Z.J.; et al. Pressure effect on superconductivity of $A_xFe_2Se_2$ (A = K and Cs). *New J. Phys.* **2011**, *13*, 033008. [CrossRef]
90. Dong, X.; Zhou, H.; Yang, H.; Yuan, J.; Jin, K.; Zhou, F.; Yuan, D.; Wei, L.; Li, J.; Wang, X.; et al. Phase Diagram of $(Li_{1-x}Fe_x)$OHFeSe: A bridge between iron selenide and arsenide superconductors. *J. Am. Chem. Soc.* **2014**, *137*, 66–69. [CrossRef] [PubMed]
91. Wu, Y.P.; Zhao, D.; Lian, X.R.; Lu, X.F.; Wang, N.Z.; Luo, X.G.; Chen, X.H.; Wu, T. NMR evidence for field-induced ferromagnetism in $(Li_{0.8}Fe_{0.2})$OHFeSe superconductor. *Phys. Rev. B* **2015**, *91*, 125107. [CrossRef]
92. Topping, C.V.; Kirschner, F.K.; Blundell, S.J.; Baker, P.J.; Woodruff, D.N.; Schild, F.; Sun, H.; Clarke, S.J. Coexistence of magnetism and superconductivity in separate layers of the iron-based superconductor $(Li_{1-x}Fe_x)OHFe_{1-y}Se$. *Phys. Rev. B* **2017**, *95*, 134419. [CrossRef]
93. Luetkens, H.; Klauss, H.-H.; Kraken, M.; Litterst, F.J.; Dellmann, T.; Klingeler, R.; Hess, C.; Khasanov, R.; Amato, A.; Baines, C.; et al. The electronic phase diagram of the $LaO_{1-x}F_xFeAs$ superconductor. *Nat. Mater.* **2009**, *8*, 305–309. [CrossRef] [PubMed]

94. Keller, H.; Bussmann-Holder, A.; Müller, K.A. Jahn–Teller physics and high-T_c superconductivity. *Mater. Today* **2008**, *11*, 38–46. [CrossRef]
95. Johnston, D.C. The puzzle of high temperature superconductivity in layered iron pnictides and chalcogenides. *Adv. Phys.* **2010**, *59*, 803–1061. [CrossRef]
96. Fang, M.-H.; Wang, H.-D.; Dong, C.-H.; Li, Z.-J.; Feng, C.-M.; Chen, J.; Yuan, H.Q. Fe-based superconductivity with T_c = 31 K bordering an antiferromagnetic insulator in (Tl,K) Fe_xSe_2. *Europhys. Lett.* **2011**, *94*, 27009. [CrossRef]
97. Wang, A.F.; Ying, J.J.; Luo, X.G.; Yan, Y.J.; Liu, D.Y.; Xiang, Z.J.; Cheng, P.; Ye, G.J.; Zou, L.J.; Sun, Z.; et al. A crossover in the phase diagram of $NaFe_{1-x}Co_xAs$ determined by electronic transport measurements. *New J. Phys.* **2013**, *15*, 043048. [CrossRef]
98. Chen, H.; Ren, Y.; Bao, W.; Liu, R.H.; Wu, G.; Wu, T.; Xie, Y.L.; Wang, X.F.; Huang, Q.; Chen, X.H. Coexistence of the spin-density wave and superconductivity in $Ba_{1-x}K_xFe_2As_2$. *Europhys. Lett.* **2009**, *85*, 17006. [CrossRef]
99. Zhang, A.-M.; Xia, T.-L.; Liu, K.; Tong, W.; Yang, Z.-R.; Zhang, Q.-M. Superconductivity at 44 K in K intercalated FeSe system with excess Fe. *Sci. Rep.* **2013**, *3*, 1216. [CrossRef] [PubMed]
100. Yan, Y.J.; Zhang, M.; Wang, A.F.; Ying, J.J.; Li, Z.Y.; Qin, W.; Luo, X.G.; Li, J.Q.; Hu, J.; Chen, X.H. Electronic and magnetic phase diagram in $K_xFe_{2-y}Se_2$ superconductors. *Sci. Rep.* **2012**, *2*, 212. [CrossRef] [PubMed]
101. Li, W.; Ding, H.; Deng, P.; Chang, K.; Song, C.; He, K.; Wang, L.; Ma, X.; Hu, J.-P.; Chen, X.; et al. Phase separation and magnetic order in K-doped iron selenide superconductor. *Nat. Phys.* **2012**, *8*, 126–130. [CrossRef]
102. Ryu, G.H.; Zhang, G.Y.; Yu, G.; Chou, M.C.; Lin, C.T. Anisotropic behavior in $(Li_{1-x}Fe_x)$OHFeSe superconducting single crystal. (Unpublished).
103. Chen, G.F.; Li, Z.; Li, G.; Zhou, J.; Wu, D.; Dong, J.; Hu, W.Z.; Zheng, P.; Chen, Z.J.; Yuan, H.Q.; et al. Superconducting properties of the Fe-based layered superconductor $LaFeAsO_{0.9}F_{0.1-\delta}$. *Phys. Rev. Lett.* **2008**, *101*, 057007. [CrossRef] [PubMed]
104. Cheng, P.; Yang, H.; Jia, Y.; Fang, L.; Zhu, X.; Mu, G.; Wen, H.-H. Hall effect and magnetoresistance in single crystals of $NdFeAsO_{1-x}F_x$ (x = 0 and 0.18). *Phys. Rev. B* **2008**, *78*, 134508. [CrossRef]
105. Palstra, T.T.M.; Batlogg, B.; Schneemeyer, L.F.; Waszczak, J.V. Thermally activated dissipation in $Bi_{2.2}Sr_2Ca_{0.8}Cu_2O_{8+\delta}$. *Phys. Rev. Lett.* **1988**, *61*, 1662–1665. [CrossRef] [PubMed]
106. Yuan, H.Q.; Singleton, J.; Balakirev, F.F.; Baily, S.A.; Chen, G.F.; Luo, J.L.; Wang, N.L. Nearly isotropic superconductivity in (Ba,K)Fe_2As_2. *Nature* **2008**, *457*, 565–568. [CrossRef] [PubMed]
107. Werthamer, N.R.; Helfand, E.; Hohenberg, P.C. Temperature and purity dependence of the superconducting critical field, H_{c2}. III. electron spin and spin-orbit effects. *Phys. Rev.* **1966**, *147*, 295–302. [CrossRef]
108. Gyorgy, E.M.; van Dover, R.B.; Jackson, K.A.; Schneemeyer, L.F.; Waszczak, J.V. Anisotropic critical currents in $Ba_2YCu_3O_7$ analyzed using an extended Bean model. *Appl. Phys. Lett.* **1989**, *55*, 283–285. [CrossRef]
109. Larbalestier, D.C.; Cooley, L.D.; Rikel, M.O.; Polyanskii, A.A.; Jiang, J.; Patnaik, S.; Cai, X.Y.; Feldmann, D.M.; Gurevich, A.; Squitieri, A.A.; et al. Strongly linked current flow in polycrystalline forms of the superconductor MgB_2. *Nature* **2001**, *410*, 186–189. [CrossRef] [PubMed]
110. Dew-Hughes, D. Flux pinning mechanisms in type II superconductors. *Philos. Mag.* **1974**, *30*, 293–305. [CrossRef]
111. Lei, H.C.; Petrovic, C. Giant increase in critical current density of $K_xFe_{2-y}Se_2$ single crystals. *Phys. Rev. B* **2011**, *84*, 212502. [CrossRef]
112. Li, M.; Chen, L.; You, W.L.; Ge, J.; Zhang, J. Giant increase of critical current density and vortex pinning in Mn doped $K_xFe_{2-y}Se_2$ single crystals. *Appl. Phys. Lett.* **2014**, *105*, 192602. [CrossRef]
113. Chen, W.; Zeng, C.; Kaxiras, E.; Zhang, Z. Dual role of Fe dopants in enhancing stability and charge transfer in $(Li_{0.8}Fe_{0.2})$OHFeSe superconductors. *Phys. Rev. B* **2016**, *93*, 064517. [CrossRef]
114. Yan, Y.J.; Zhang, W.H.; Ren, M.Q.; Liu, X.; Lu, X.F.; Wang, N.Z.; Niu, X.H.; Fan, Q.; Miao, J.; Tao, R.; et al. Surface electronic structure and evidence of plain s-wave superconductivity in $(Li_{0.8}Fe_{0.2})$OHFeSe. *Phys. Rev. B* **2016**, *94*, 134502. [CrossRef]
115. Du, Z.; Yang, X.; Fang, D.; Du, G.; Xing, J.; Yang, H.; Zhu, X.; Wen, H.H. Scrutinizing the double superconducting gaps and strong coupling pairing in $(Li_{1-x}Fe_x)$OHFeSe. *Nat. Commun.* **2016**, *7*, 10565. [CrossRef] [PubMed]